

# POLITECNICO DI TORINO

Collegio di Ingegneria Civile

Corso di Laurea Magistrale in Ingegneria Civile

Tesi di Laurea Magistrale

## Influence of Bi-material interface on the onset of dynamic rupture



### Relatori

Prof. Sebastiano Foti

Prof.ssa Marie Violay

Dr. François X. Passelègue

**Candidato**

Federica Paglialunga

Ottobre 2018



*Ai miei nonni.*



# Abstract

The elastic strain energy stored in the upper crust is released locally along faults through different slip modes, ranging from stable slip with no associated radiations to fast and destructive earthquakes. Understanding the physical processes involved and the conditions allowing the transition between these different slip modes is crucial because earthquake damage increases with rupture velocity [22, 12]. While numerous studies focused on the understanding of the nucleation and the propagation of rupture of homogeneous interface, natural faults often present an asymmetric distribution in damage and lithology. Based on numerical results [3, 40], we know that material contrast plays an important role in controlling the rupture propagation along the interface. In particular, rupture is expected to propagate preferentially in one direction, following the more compliant material slip direction.

The purpose of this work was to investigate for the first time the influence of material contrast on the frictional behaviour of the interface, as well as the propagation of dynamic rupture. Two kinds of contrast were investigated: (i) asymmetric roughness and (ii) asymmetric lithology. Frictional behaviour was studied using Strassentest simple shear apparatus. Dynamic rupture experiments were conducted using a Hopkinson shear apparatus. Ruptures generated during experiments were monitored using pressure transducers, coupled with strain gages and acoustic high-frequency monitoring systems. Our results demonstrate that while both materials exhibit velocity-weakening behaviour, the frictional behaviour of the bimaterial interface depends on the material contrast as well as on the interface roughness. During dynamic rupture, the dynamic stress drops result in an average of both material. This result seems in agreement with dynamic rupture experiments. Our results about rupture propagation at the onset of slip agree with numerical results obtained by [3, 40]. The rupture nucleates at the edge of the fault and propagates preferentially in the slip direction of the softer medium.



# Acknowledgments

Firstly I would like to thank Dr. Francois Passelgue for his guidance through this work. His unlimited patience and willingness to help me and teach me so much, really supported me in these months. I would like to thank Professor Marie Violay and Professor Cino Viggiani, for giving me this great opportunity to do this reasearch project at EPFL, I am really grateful to both of them. Then, I would like to thank Professor Sebastiano Foti for being my supervisor from Politecnico of Turin. I say *infinite grazie* to Dr. Carolina Giorgetti for sharing her knowledge with me and for spending so much of her time giving me very valuable advices. I also want to thank the whole LEMR at EPFL (Laboratory of experimental rock mechanics) for infecting me, everyone in his own way, with their passion for research (and rocks!). I say thank you to all the MGCER class 2018 students, because getting to know each of them made the world feel much smaller than it is.

*Passando ora dalla lingua dello studio a quella del piacere per i ringraziamenti del cuore, dico grazie alla mia famiglia. Grazie a mamma per avermi sempre coccolato, pronta ad adattarsi ad ogni mezzo per raggiungere lo scopo, troppo spesso dovendosi accontentare di un telefono; a papà per avermi spronato a fare cose che io nemmeno quasi speravo di riuscire a fare; alla mia sorellina per avermi fatto divertire anche nei momenti pi tristi, per avermi confortato prima di ogni esame, unica complice costretta al patto del silenzio. Senza il vostro supporto sarebbe stato tutto molto piú difficile.*

*Grazie a tutti gli amici che ho incontrato lungo questo percorso. Fortunatamente sono stati tanti e provenienti da un po' ovunque. Ringrazio tutti loro per aver condiviso con me questo percorso, che mi ha vista crescere anche per merito vostro.*

*Grazie anche a chi non vede il proprio nome scritto su questo foglio, perché a stamparlo con dell'inchiostro si sciuperebbe. La sua vicinanza durante questi ultimi mesi stata energia per continuare e concludere questo mio lavoro al meglio di ciò che potevo.*



# Contents

<b>1</b>	<b>Introduction</b>	<b>1</b>
1.1	Spring block-model as an analogue for earthquakes . . . . .	1
1.2	Frictional laws governing rupture nucleation . . . . .	3
1.3	Propagation of dynamic rupture front . . . . .	4
1.4	Influence of bi-material on onset of dynamic instabilities . . .	5
1.5	Objective of this master thesis . . . . .	5
<b>2</b>	<b>Material and Methods</b>	<b>9</b>
2.1	Sample preparation . . . . .	9
2.2	Stressentest Apparatus . . . . .	12
2.3	Hopkinson 2D Apparatus . . . . .	13
<b>3</b>	<b>Bimaterial interface on friction law parameters. Stressentest</b>	<b>17</b>
3.1	Experimental results . . . . .	17
3.1.1	Stable sliding behaviour . . . . .	18
3.1.2	Stick-slip tests . . . . .	21
3.2	Discussion. . . . .	29
<b>4</b>	<b>Propagation of rupture. Hopkinson 2D</b>	<b>33</b>
4.1	Experimental results . . . . .	33
4.2	Estimation of local strain and stress along the fault plane . .	34
4.3	Analysis of acoustic data . . . . .	37
4.4	Interpretation and discussion . . . . .	40
4.4.1	Comparison between stress distribution and rupture nucleation . . . . .	40
4.4.2	Interpretation of stress heterogeneity . . . . .	46
4.4.3	Effect of directivity. . . . .	48
4.4.4	Future prospects . . . . .	48
<b>5</b>	<b>Conclusions</b>	<b>51</b>
<b>A</b>	<b>Hopkinson 2D configuration</b>	<b>53</b>

<b>B Hopkinson 2D - Defining strain and stress tensor.</b>	<b>59</b>
B.1 Strain tensor . . . . .	59
B.2 Stress tensor correction . . . . .	60

# List of Figures

1.1	Scheme of the spring-block system. . . . .	2
1.2	a. Evolution of the friction coefficient with slip for the slip-weakening friction law. b. Evolution of the friction with the slip for the Rate and State friction law. . . . .	3
1.3	Modes of rupture [20]. . . . .	5
1.4	Profile of slip and slip velocity along the fault at different times ([38]). (a.) homogeneous case. (b.) interface with a material contrast of 5% . . . . .	6
2.1	Two samples of Gabbro (on the left) and Granite (on the right). . . . .	9
2.2	Picking of arrival times for P waves and S waves for Gabbro (top pannel) and Granite (bottom pannel). The squares identify the P waves arrival while the circles identify the S waves arrival. . . . .	11
2.3	STRESSENTEST shear apparatus in LEMR, EPFL. . . . .	13
2.4	Scheme of shear apparatus (top figure). Stiffness of the shear apparatus (bottom figure). . . . .	14
2.5	Hopkinson 2D configuration. Top view. . . . .	15
3.1	Granite-grid60 at 1MPa and 0.25 MPa. . . . .	18
3.2	(a.) Evolution of friction with the horizontal displacement (test RS06). Seven velocity steps were imposed. (b.) Comparison between experimental data obtained during a velocity step and the results of the inversion of the rate and state parameters, conducted following the inversion code FSS 7.1 [25] (test RS06). . . . .	19
3.3	Velocity steps imposed during the test. . . . .	20
3.4	(a.) Evolution of the friction with the displacement for Gabbro and Granite (RS06, RS09). Seven velocity steps were imposed. (b.) (a-b) values computed both manually and modelled through FSS 7.1 inversion code. . . . .	20

3.5	(a.) Evolution of the friction with the displacement for the bimaterial interface Gabbro-Granite (RS08). Seven velocity steps were imposed. (b.) (a-b) values computed both manually and modelled through FSS 7.1 inversion code. . . . .	21
3.6	(a.) Unstable behaviour of Granite (grid 600) (Stick slip). (b.) Force drops vs peak shear load reached by each single drop. (c.) Evolution of friction with the logarithm of the sliding velocity. . . . .	22
3.7	(a.) Stick-slip sequence observed during an experiment on $Gab_{smooth}$ . (b.) Force drops vs peak shear load reached at each single event. (c.) Evolution of friction with the logarithm of the sliding velocity. . . . .	22
3.8	Effect of roughness on monomaterial interface. . . . .	24
3.9	Effect of bimaterial. . . . .	25
3.10	Combination of bimaterial and biroughness effects. . . . .	25
3.11	Scheme of the mechanical system spring-block. . . . .	26
3.12	Evolution of upper and lower values of friction. . . . .	30
3.13	Evolution of static and dynamic values of friction. . . . .	30
4.1	Mechanical results of the two applied loads; normal load and shear load. Evolution of the acoustic emissions with time. Are reported the three experiments: T10 (Gabbro-Gabbro), T13 (Granite-Granite), T12 (Gabbro-Granite). . . . .	35
4.2	Evolution of stress along the fault test T10. . . . .	36
4.3	Location of AEs during experiments. . . . .	38
4.4	T10, Gabbro-Gabbro. Acoustic waveform along the fault for four events. In red rupture propagation. . . . .	40
4.5	T13, Granite-Granite. Acoustic waveform along the fault for four events. In red rupture propagation. . . . .	41
4.6	T12, Gabbro-Granite. Acoustic waveform along the fault for four events. In red rupture propagation. . . . .	41
4.7	Rupture propagation velocity for T10, T13, T12. . . . .	42
4.8	Test T10 (Gabbro-Gabbro). (a) Rupture propagation front from acoustic data. (b) Stress distribution along the fault, prior the event. (c) Stress drops distribution recorded for each location along the fault. . . . .	43
4.9	Test T13 (Granite-Granite). (a) Rupture propagation front from acoustic data. (b) Stress distribution along the fault, prior the event. (c) Stress drops distribution recorded for each location along the fault. . . . .	44
4.10	Test T12 (Gabbro-Granite). (a) Rupture propagation front from acoustic data. (b) Stress distribution along the fault, prior the event. (c) Stress drops distribution recorded for each location along the fault. . . . .	45

4.11	Evolution of shear stress and global friction with time. On the plot the precursory events and the main events are pointed out in blu. . . . .	47
4.12	Scheme of rupture propagation in a bimaterial interface with softer medium put at the bottom. . . . .	48
A.1	Picture of the Hopkinson 2D apparatus, LEMR-EPFL. . . . .	54
A.2	Configuration of the Hopkinson 2D machine . . . . .	54
A.4	(Top figure) Configuration of the machanical sensors placed along the fault. Strain gages are glued on the upper block. (Bottom figure) Strain rosette used as mechanical sensor, which records strain in three directions; n1 which is parallel to y, n3 which is inclined by 45 degrees and n2 which is inclined by 135 degrees. . . . .	55
A.5	Configuration of the acoustic sensors placed along the fault. Acoustic sensors are glued on the lower block. Unite measure: mm. . . . .	55
A.6	Configuration of the mechanical and acoustic sensors. In this specific case the lower sample broke during the testing because of an alignment issue. . . . .	56
A.7	Different configuration of the mechanical and acoustic sensors in order to choose the best one for our needs. On the thickness of the sample some stripes can be observed. . . . .	57
A.8	Sample from one of the last experiments with the machine in its upgraded configuration. On the thickness of the sample some stripes can be observed. They are not distributed uniformly along the interface. This is sign of the influence of edge effect. . . . .	58
B.1	Strain rosette in three directions; n1 which is parallel to y, n3 which is inclined by 45 degrees and n2 which is inclined by 135 degrees. . . . .	60
B.2	Stress equilibrium. . . . .	61



# Chapter 1

## Introduction

Faults and fractures release the elastic strain energy stored in the earth crust through different modes of deformation, going from slow slip earthquakes [16] which are localized slip events (sometimes up to moment magnitudes of Mw 7.5) that propagate too slowly (km/days) to radiate elastic waves, up to regular and supershear earthquakes [21, 8] where the rupture velocity exceeds the shear wave velocity (km/s). However, the physical processes involved and the environmental conditions allowing the transition between these different earthquake rupture speeds remain poorly understood. However this is of crucial importance because earthquake damages mostly depend on the rupture front speeds [22, 12]. Those earthquakes nucleate within the seismogenic portion of the crust.

The upper limit of the seismogenic zone, (at about 3-4 Km) is governed by the frictional properties (transition from slip strengthening to slip weakening regime) of the fault whereas the bottom limit of seismogenic zone is controlled by a transition in fracture mode, from brittle ductile deformation [10, 15], (10-to-15 km depth).

### 1.1 Spring block-model as an analogue for earthquakes

In the past decades, numerous laboratory experiments have been conducted to improve our understanding of earthquake mechanics and help us to better characterize the different rupture speeds and slip modes observed in nature. This approach is underlined in the work of (i) Byerlee and Brace [9, 11], who first proposed the mechanism of stick-slip as an analogue for earthquakes, then (ii) in the work of Scholz and Johnson [19, 18] who investigated the earthquake source parameters in the laboratory, and finally (iii) in the work of Ohnaka [26] who described the complete mechanism of stick slip, from nucleation to dynamic propagation of rupture.

A stickslip event is divided in two different stages. In a first phase the

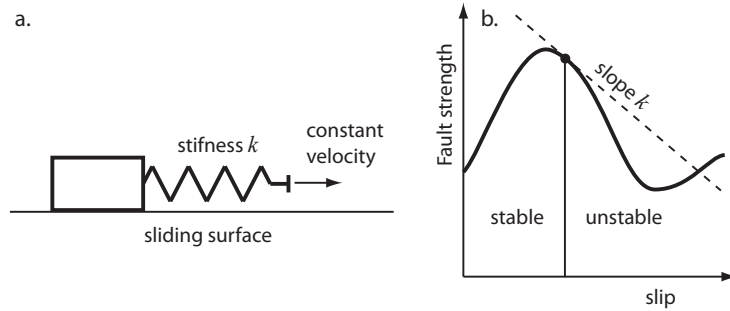


Figure 1.1: Scheme of the spring-block system.

two surfaces *stick* together, allowing the accumulation of elastic strain in the medium due to the loading of the fault system up to a critical stress, which corresponds to the peak strength of the fault, commonly defined by the static friction coefficient. When the stress reaches this critical value, a sudden *slip* occurs. The slip stage is due to the rupture of the fault interface, which induces the release of the strain accumulated within the medium during the loading stage. This sequence can be repeated in a cycle manner in time. Stick-slip behaviour can be modelled by a simple *spring-block* system (1.1).

In such system, the stability of the fault is a function of (i) the stiffness of the spring  $K$  which corresponds to the stiffness of the surrounded medium of the fault and (ii) the stiffness of the fault which is defined by the evolution of the friction with increasing slip. If the strength of the fault was given by Fig. 1.1 (b), two different scenarios can occur at the onset of slip. (i) The fault strength decreases slower than the machine stiffness. In this case, the energy release can be absorbed by the medium, and the slip stage remains stable. (ii) The fault strength decreases faster with slip than the machine stiffness. In such cases, the energy is released faster than what the system can absorb, inducing the radiation of elastic waves during the slip stage. Following this, it is possible to determine if a system will behave in a stable or unstable way using the following relationship ([36]):

$$\frac{\partial F}{\partial u} > K \quad (1.1)$$

where  $F$  is the shear force,  $u$  is the slip and  $K$  the machine stiffness. Following this relation, the stability of the fault system is mostly controlled by the frictional history of the fault during the slip stage. This frictional history is commonly defined by frictional aging law.

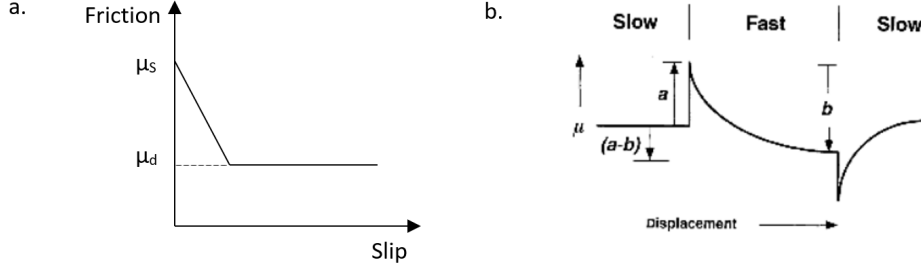


Figure 1.2: a. Evolution of the friction coefficient with slip for the slip-weakening friction law. b. Evolution of the friction with the slip for the Rate and State friction law.

## 1.2 Frictional laws governing rupture nucleation

To describe frictional behaviour between two sliding surfaces, two friction laws are commonly used (Fig. 1.2);

- Slip-weakening law
- Rate and state law.

Rate and State friction law is the most common law used to model the response of a frictional interface submitted to a stress or strain perturbation. This constitutive law considers not only a static and a dynamic friction coefficient, but can describe and explain the evolution of the frictional strength during the slip stage [31]. The variables characterizing this kind of behaviour are the shear stress, the normal stress, the slip rate and the asperity contact. This theory describes how stick-slips occur and the frictional changes that permit this. In a particular way frictional behaviour can be described by Eq. 1.2, by means of the three following parameters:  $a$ ,  $b$ ,  $D_c$

$$\tau = \sigma_n \left[ \mu_0 + a \cdot \ln\left(\frac{V}{V_0}\right) + b \cdot \ln\left(\frac{V_0 \theta}{D_c}\right) \right] \quad (1.2)$$

with  $\theta$  a state variable which is related to  $V$  and  $D_c$  as it follows (slip law):

$$\frac{\partial \theta}{\partial t} = 1 - \frac{\theta V}{D_c} \quad (1.3)$$

[23], Dieterich [14] came up with the idea that the state variable  $\theta$  could be seen as an average contact life, with time dimensions given by  $\frac{D_c}{V}$ .

These parameters can be determined by imposing velocity steps during stable slip friction experiments. At each velocity step, the fault will respond with an increase (or decrease) of friction called *direct-effect* which corresponds to parameter  $a$ . Then, friction will start decreasing until it reaches a new stable value (dynamic friction coefficient). The difference between this

stable value and the previous peak is called parameter  $b$ . The distance  $D_c$  represents the distance required to reach the stable value. These parameters are of remarkable importance in defining frictional stability of a fault. Indeed, if  $(a-b) > 0$  the fault behaviour will be stable and in particular it will be called **velocity-strengthening** behaviour. If  $(a-b) < 0$  the behaviour will promote unstable mode of slip, also called **velocity-weakening** behaviour.

These frictional parameters can be used to determine [34] the stiffness of the fault, which is given by the following equation:

$$K_C = \frac{(b - a) \cdot \sigma_N}{D_C} \quad (1.4)$$

As stated previously in the description of the spring-block model:

- If  $K > K_C$  then the system will behave stably;
- If  $K < K_C$  then the system will behave unstably.

### 1.3 Propagation of dynamic rupture front

Once the rupture nucleates, following the stability criteria described before, one supplementary criterion is requested for earthquake propagation: friction has to drop from the static to the dynamic value in a very abrupt and dynamic manner. If this happens, then a dynamic rupture can propagate on the frictional interface. For what concerns the rupture itself, it is well known that there are three crack propagation modes: Mode I (opening mode), Mode II (shear in plane mode), Mode III (shear in anti-plane mode). Given the conditions at which rocks are subjected most of the time, the bigger attention is put in the observation (at a macroscopic scale) of Mode II and Mode III. This distinction is very useful not only to understand the displacement evolution along the crack, but also because depending on the rupture mode, different rupture velocities can be reached. In fact, while in Mode III rupture cannot propagate faster than  $V_S$  (S wave velocity), in Mode II it becomes possible having ruptures that travel at *Supershear* velocity. The supershear ruptures can propagate at velocities in between  $V_S$  and  $V_P$  (P wave velocity).

It was noticed [5], [28] that the rupture mode and the rupture velocity depend on the stress orientation and stress ratio:  $\frac{\tau(x)}{\sigma(x)}$ . In particular it turns out that slow fronts occur for values lower than 0.5, sub-Rayleigh fronts for values between 0.5 and 0.8 and supershear fronts for values greater than 0.8. Along the fault, due to the non-uniformity of contact and stresses there will be different values of  $\frac{\tau(x)}{\sigma(x)}$ . This will for sure affect the propagation of the

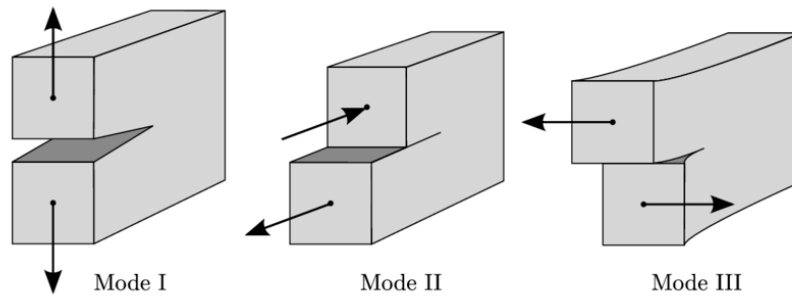


Figure 1.3: Modes of rupture [20].

front which can slow down, arrest or speed up depending on what it will find on the path.

## 1.4 Influence of bi-material on onset of dynamic instabilities

While recent studies generally focus on the understanding of rupture processes along mono-material interface, little attention was given to the influence of bi-material interface on the onset of instabilities. However, understanding dynamic rupture in a bi-material interface is of great importance since most of the seismogenic natural faults present an asymmetry in the elastic properties, roughness or in damage distribution. According to [3, 40], rupture propagates preferentially in one direction, following the more compliant material slip direction. This has been confirmed by numerical studies [38] which show that in bi-material interfaces, rupture propagates faster in the direction of slip of the side of the fault which is more compliant (Fig. 1.4).

Another important factor in bi-material interfaces is the coupling of the slip with the normal stress. For mono-material faults this coupling does not exist, but for bi-material ones a *climb motion* [40] generates in the perpendicular direction of propagation, which causes a normal traction stress. This normal traction stress is also called 'short-range' stress because it exists only where the dislocation generates.

## 1.5 Objective of this master thesis

The purpose of this master project was to study the frictional behaviour and so nucleation and propagation of dynamic rupture along a bi-material rock

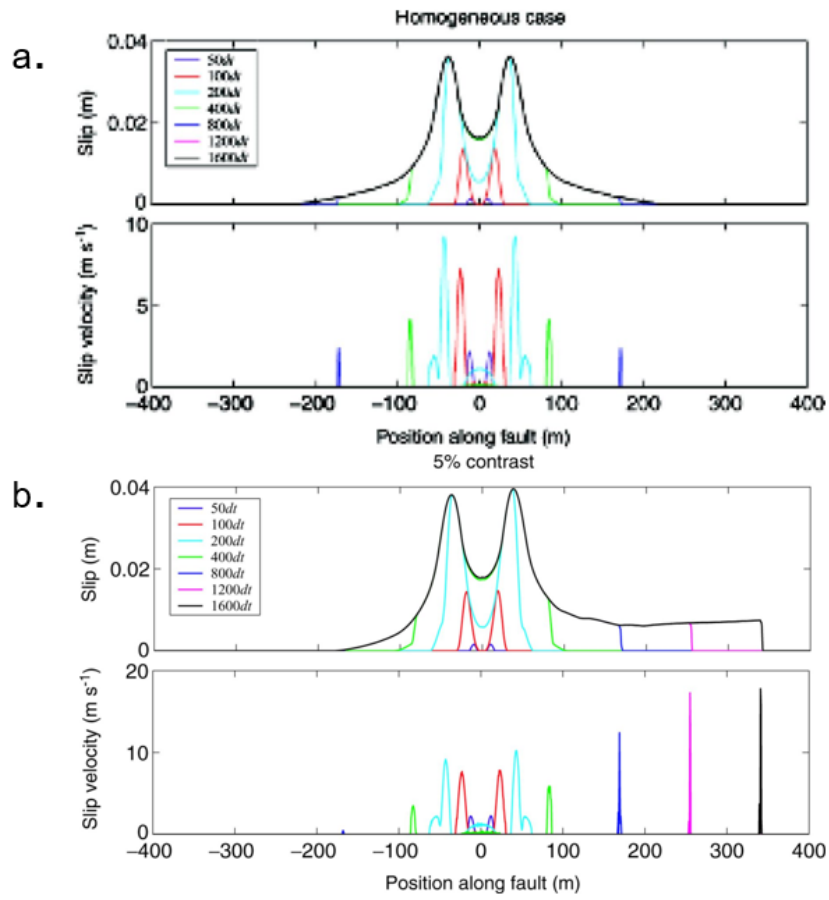


Figure 1.4: Profile of slip and slip velocity along the fault at different times ([38]). (a.) homogeneous case. (b.) interface with a material contrast of 5%

interface under quasi-static and dynamic conditions.

The frictional behaviour was analysed using a single direct shear machine (STRESSENTEST) with which I studied the frictional behaviour of interface presenting an asymmetry in roughness and in lithology. Frictional and rupture processes were investigated from both stable and unstable events, allowing to defining rate and state parameters [34].

A special attention in this study was put on the influence of a bi-material interface on the propagation of rupture as well. In order to study these processes, I helped to develop a large biaxial Hopkinson apparatus. The objective was to try to understand how a rock interface, and mostly a bi-material rock interface responds to an external solicitation. A strong part of this thesis was dedicated in the development of the acquisition system and the set up of the machine. To improve the configuration of the apparatus, more than 70 experiments were conducted.

While only the results of three experiments (for the Hopkinson 2D part) are presented in what follows, the results of each experiment run was processed in order to adjust in an iterative way the machine and to get to this last configuration. The experiments were recorded with strain gages and acoustic sensors so that the strain and stress states could be computed in time and along the fault.



## Chapter 2

# Material and Methods

### 2.1 Sample preparation

The two rocks used in this study were selected due to their simple composition, medium grain size and homogeneous and isotropic characteristics making them perfect for experimental study: a black Gabbro and coarse grained Granite. Both are magmatic intrusive rocks. Granite has a high content of quartz ( 72.04%  $SiO_2$ ) and feldspar. Gabbro has a lower content of quartz and mostly consists in plagioclase ( $45% < SiO_2 < 52%$  ).

**Dynamic elastic properties.** The two materials present different elastic properties making them suitable for the study of a bi-material interface and for observation of directivity effect.

As we know [1], inside a medium strain transfers through elastic waves. In particular we can distinguish strain [1] between a *scalar cubic dilatation* and a *vector shear strain*, which are strictly related to P waves (Primary) and S waves (Secondary). This is the reason why to estimate the elastic properties of a medium, it is important to refer to these two elements.

The source of these elastic waves can be either natural or artificial. To measure the P and S wave velocities in the lab it is used an artificial source. Both



Figure 2.1: Two samples of Gabbro (on the left) and Granite (on the right).

	Velocity [m/s]
P waves	6560
S waves	4078

Table 2.1: Determination of P and S wave velocities for Gabbro.

	Velocity [m/s]
P waves	5634
S waves	2991

Table 2.2: Determination of P and S wave velocities for Granite.

P and S wave velocities were measured at room pressure and room temperature using P and S wave transducers provided by Farnell instruments. These sensors present a frequency response in the order of 2 MHz, allowing measurement of elastic wave velocity through a small specimen. A voltage pulse was induced using a generator and an amplifier, allowing a sinusoidal pulse presenting a period of 50 microseconds and an amplitude of 100 Volts. By picking the P and S arrival times, elastic velocities were computed following these relationships:

$$V_P = \frac{w}{t_P} \quad (2.1)$$

$$V_S = \frac{w}{t_S} \quad (2.2)$$

with  $w$  being the sample's width.

The data can be seen in Tab 2.1 and 2.2

The Poisson coefficient was obtained by the following equation 2.3, being dependent only on P and S waves velocities:

$$\nu = \frac{[\frac{1}{2} \cdot (\frac{V_P}{V_S})^2 - 1]}{[(\frac{V_P}{V_S})^2 - 1]} \quad (2.3)$$

The density of the rocks was estimated by weighing the sample whose volume was measured as well. By dividing the mass of the sample by its volume the estimated values for the density of Gabbro and Granite were given. Once known the density, the values of the two moduli could be defined through the following:

$$G = V_S^2 \rho \quad (2.4)$$

$$E = 2(1 + \nu)G \quad (2.5)$$

Finally summarising the elastic properties of the materials are shown in Tab. 2.3

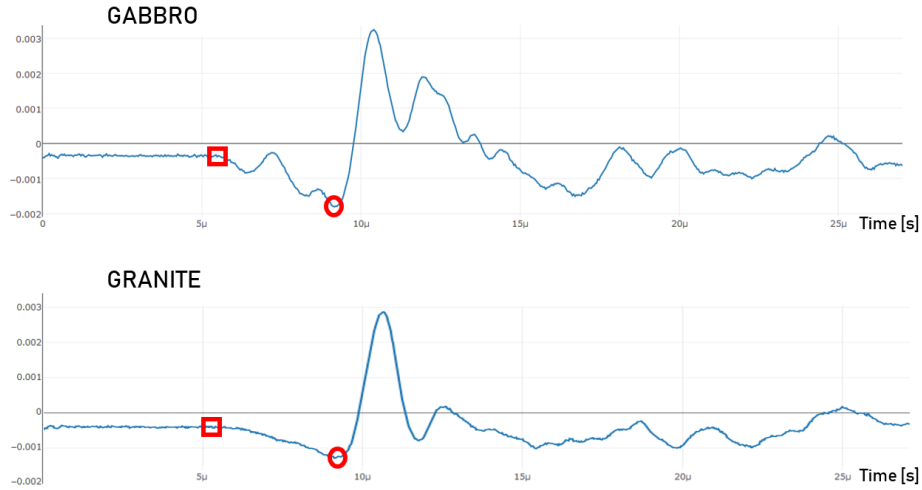


Figure 2.2: Picking of arrival times for P waves and S waves for Gabbro (top panel) and Granite (bottom panel). The squares identify the P waves arrival while the circles identify the S waves arrival.

	Gabbro	Granite
$V_P$ [ $\frac{m}{s}$ ]	6560	5634
$V_S$ [ $\frac{m}{s}$ ]	4078	2991
E [GPa]	88.3	64.3
$\nu$	0.244	0.215
$\rho$ [ $\frac{g}{m^3}$ ]	$2.898 \cdot 10^6$	$2.608 \cdot 10^6$

Table 2.3: Properties of Gabbro and Granite used in this study.

**Material contrast.** The material contrast is a value that describes how much two different material differ one from the other, in particular in terms of elastic properties. In this specific case it is estimated through the following:

$$MC = \left( \frac{\rho_{gabbro}}{\rho_{granite}} - 1 \right) 100[\%] \quad (2.6)$$

A contrast of  $\approx 10\%$  in the elastic properties is observed.

This contrast allows us to differentiate the influence of both materials within the rupture processes, and it is expected to induce an sufficiently strong, or at least observable, directivity effect.

## 2.2 Stressentest Apparatus

In order to study the frictional behaviour of the rocks used in this study, direct shear experiments were carried out using a single direct shear apparatus (STESSENSTEST). For this kind of test two rectangular samples were used with the following dimensions: 5.6 cm x 7.6 cm x 2.0 cm. In order to run the test they had to be locked in two frames which could allow them to slide one respect to the other. For both materials the samples were prepared in the same way. First they were rectified using a grinder apparatus, insuring a misalignment smaller than 200 microns/meter. The wanted roughness was then applied using appropriated sandpaper. In this manuscript, we choose to present the results of experiments conducted at two different roughness obtained using sandpaper referenced as P60 and P600, which promote an average grain size of 250 microns and 25 microns respectively.

Experiments were conducted at different normal loads, which were imposed to be constant during each experiment. The desired normal load was imposed by placing some weights hanging on a beam that transfers all the force on the sample surface through a lever mechanism it. In detail the lever *load arm* has a length of 5 cm and the *effort arm* has a length of 50 cm. The applied force on the sample (by computing the momentum equilibrium around the fulcrum) is given by:

$$F_N = m \cdot a_g \cdot \frac{l_{effort}}{l_{load}} = m \cdot a_g \cdot 10 \quad (2.7)$$

Two masses have been used in the experiments:

- 47 kg which corresponds to a normal force equal to 4610 N (when an unstable behaviour was required)
- 7 kg which corresponds to a normal force equal to 687 N (when an stable behaviour was required).

All experiments were conducted using the same protocol. A first given slip velocity was imposed at the initiation of the loading up to the onset of slip thanks to a step motor connected to the upped box. Then, velocity jumps

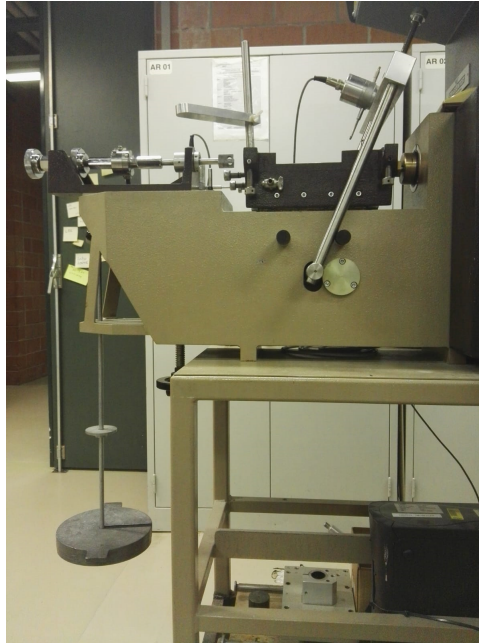


Figure 2.3: STRESSENTEST shear apparatus in LEMR, EPFL.

were imposed to study the influence of the slip velocities on the frictional properties of the fault interface. The output values are the shear stress, horizontal and vertical displacements. The shear stress was measured by a load cell, while the two displacements were measured by two LVDTs. Mechanical data were recorded at a sampling rate of 300 Hz during the entire experiments, independently of the slip velocity.

**Fault's stiffness.** A machine calibration was carried out, to evaluate the stiffness of the apparatus. The experiment was run with a steel block instead of the normal sample, measuring the shear force changing in dependence on the displacement (Fig.2.4). Three different tests were run at different applied normal stresses. The stiffness of the machine was estimated in the range of 3400 N/mm. Mechanical outputs obtained from the experiments were systematically corrected using the following:

$$\frac{1}{K_{system}} = \frac{1}{K_{apparatus}} + \frac{1}{K_{sample}} \quad (2.8)$$

## 2.3 Hopkinson 2D Apparatus

While single shear apparatus allows to study the frictional properties of fault interfaces, the study of the dynamic rupture processes requires the record at high frequency of both strain and stress along the interface. To study

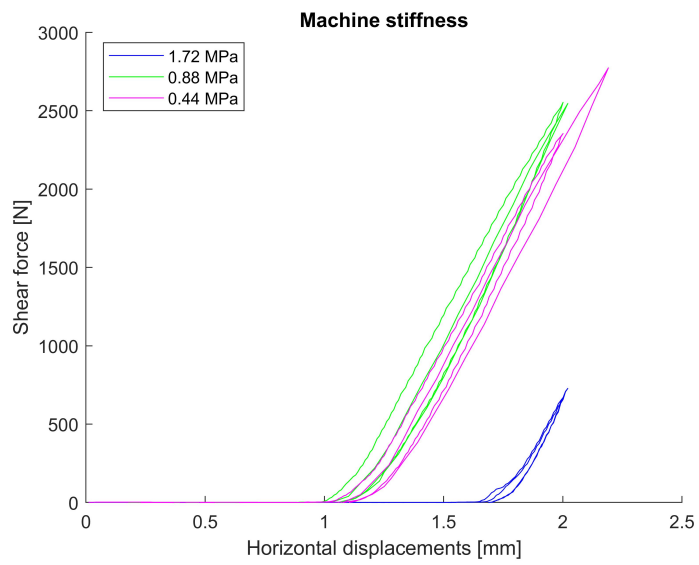
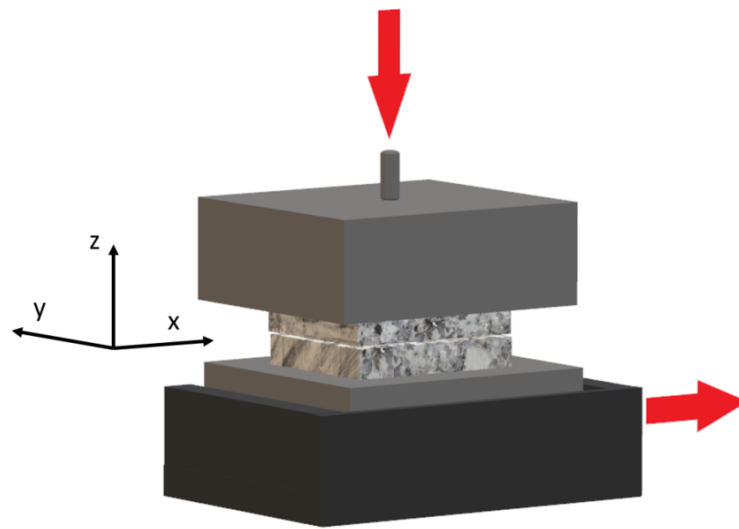


Figure 2.4: Scheme of shear apparatus (top figure). Stiffness of the shear apparatus (bottom figure).

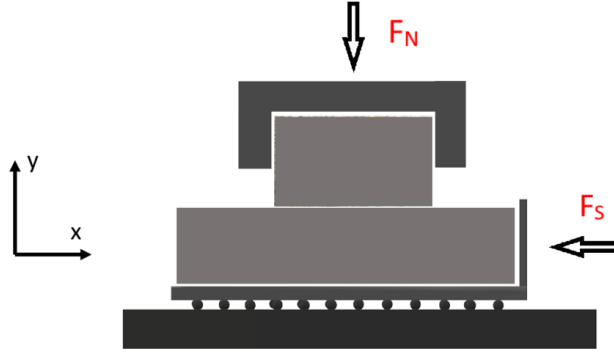


Figure 2.5: Hopkinson 2D configuration. Top view.

Material	Gabbro	Granite
Upper block	14.5 x 20.0 x 3.00 $cm^3$	15.2 x 20.0 x 2.70 $cm^3$
Lower block	12.0 x 50.0 x 3.00 $cm^3$	12.0 x 43.5 x 2.70 $cm^3$

Table 2.4: Dimensions of the four samples used for Hopkinson 2D.

these processes, a two dimensions Hopkinson apparatus was developed and configured in a single shear configuration i.e. the two samples slide one on the other. The external loading was imposed using two enerpacs allowing to apply a maximum stress of 200 bars. The normal load was applied to the upper sample and the shear load was applied on the bottom sample (Figure 2.5). The normal load was applied using a servo controlled hydraulic pump which allowed to keep regulate a constant value of normal stress during the loading stage of the experiment. In contrary, the pump used to apply the shear load was a hand pump. The maximum horizontal displacement (which corresponds to the maximum slip of the fault) was of 3 cm.

The two blocks were both very thin, reason why it has been made the hypothesis that the rupture would propagate in one direction along the interface.

The dimensions of the samples used in the tests are in Table 2.4.

**Mechanical recording system** Mechanical data were recorded using two different types of sensors. The evolution of both shear and normal stresses were recorded using two load cells located between the enerpacs and the samples. In addition to the load cells, the complete strain tensors were measured at seven location along the fault using strain gauges (Fig. A.4 and A.5). The strain gauges (product type: BX120-10AA), which were bought from the Zhejiang Huangyan Testing Apparatus Factory, China, have a sense organ size of 10 mm (long) by 5 mm (width). The strain gauges were connected in the Wheatstone quarter-bridge to measure axial strain and to reject bending strain. This strain gauge connection could also reduce signal noise and

make the recorded signal smooth. The sampling rate was 50 kHz, which is the minimum by the acquisition card. The strain gages used were strain rosettes (Fig A.4) with nominal strain resistance of  $120 \pm 0.5 \Omega$  and a gage factor of  $2.09 \pm 1$ . The deformation was monitored on each strain gage of the rosette by completing the quarter bridge by three additional strain gages within the acquisition cards, depending on the nominal gage resistance and gauge factor. The same DAQ (Data Acquisition system) was used to monitor the record of the 21 strain gages located along the fault, as well as the two load cells using the software LabVIEW. The sampling frequency was 50kHz, giving a measurement each  $20 \mu s$ . Raw data were low-pass filtered to remove high frequency noise with Savitzky- Golay filter MATLAB function.

**Acoustic recording system** In order to monitor acoustic emissions during experiments, piezoelectric sensors were glued on the rock surface using cyanocrylate adhesive. Eleven sensors were used in this study. The piezo-ceramic sensors used consist of a PZT crystal (PI ceramic Pi255, 5 mm in diameter and 0.5 mm in thickness) encapsulated within a brass casing. All the piezoelectric crystals were polarized in the same way and record preferentially shear waves. The signal received on each sensors was then relayed through coaxial cables. A classic sensor array used during experiments is displayed in FigA.4. These eleven acoustic S-wave sensors were connected to the 11 channels of the recording system. In a first output, the unamplified signal was relayed to a 11 channel digital oscilloscope, at a sampling rate of 10 MHz. The signal was recorded only if it verified a given pattern (i.e., a threshold amplitude on a given number of channels in a given time window). This way of recording was used to be sure to record the waveforms corresponding to macroscopic dynamic events during experiments i.e., rupture of the entire fault). The measurement of the unamplified signals allowed the record of unsaturated waveforms corresponding to the particle accelerations during dynamic rupture propagation [37, 28]. Using a second system, signals were amplified at 45dB via 11 pre-amplifiers. The amplified signals were then relayed to a trigger logic box and, if verifying a given pattern (i.e., a threshold amplitude on a given number of channels in a given time window), are relayed and recorded by a second 11 channel oscilloscope, allowing to record the acoustic waveforms during the entire experiments at 10 MHz sampling rate. The complete waveforms were then analysed and cut into single AE when the signals verify a given pattern. This system was used to record the complete AE waveforms catalogs during experiments while the "triggered data system" was limited to 10 AEs /second.

## Chapter 3

# Bimaterial interface on friction law parameters. Stressentest

In the last decades many studies focused on the understanding of the mechanisms controlling the evolution of the frictional strength during earthquake sliding from an experimental and a theoretical point of view [34, 31, 23, 24, 35]. These studies highlighted that friction evolution can be described by rate-and-state frictional law through three independent parameters ( $a$ ,  $b$ ,  $D_c$ ). This law reproduces the entire seismic cycle, from the nucleation to the propagation of instabilities. Most of the recent studies focused on the understanding of the evolution of the friction along mono-material faults. Here, in the first part of this thesis, the focus was put on the influence of roughness and bi-material on the frictional behaviour, and notably on rate-and-state parameters.

### 3.1 Experimental results

Using the Stressentest shear apparatus, various combinations were tested such as stress conditions, initial roughness and lithology to study the stress and rate dependence of the bi-material interface on friction. As seen before the two used materials were Gabbro and Granite. Various roughness's were tested, imposing various velocity histories. Different roughness's were imposed using sandpaper with different grids. The difference between the two roughness's could be observed at naked eye. We call rough and smooth surfaces, the surfaces prepared with a of grid P60 and P600, respectively. To test the reproducibility of the experiments, most of them were run twice, to make sure that the results were reproducible.

1 MPa	0.25 MPa
Unstable sliding (stick-slip)	Stable sliding

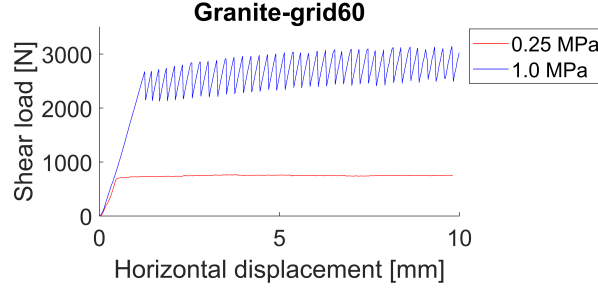


Figure 3.1: Granite-grid60 at 1MPa and 0.25 MPa.

With these two grids different combinations were tested such as:  $Gab_{rough}$ - $Gab_{rough}$ ,  $Gra_{rough}$  -  $Gra_{rough}$ ,  $Gab_{rough}$  -  $Gra_{rough}$ ,  $Gra_{rough}$  -  $Gab_{rough}$  (to check for side effects),  $Gab_{smooth}$  -  $Gra_{smooth}$ ,  $Gab_{rough}$  -  $Gab_{smooth}$ ,  $Gra_{rough}$ -  $Gra_{smooth}$ .

Two different normal loads corresponding to a stress of 0.15 and 1 MPa, were applied. For all the conditions tested, it was possible to systematically observe stable slip behaviour at the lower stress conditions, while higher stress conditions induced the transition from stable to unstable slip, with resulting stick-slip events. Results obtained during stable slip experiments were used to analyse the frictional parameters of the interfaces, and stick-slip sequences were used to study the dynamic processes of instabilities. 3.1.

### 3.1.1 Stable sliding behaviour

As stated previously, stable slip behaviour was systematically observed at low normal stress conditions, mostly on rough interfaces ( $Gab_{rough}$  and  $Gra_{rough}$ ). For each experiment, the strength of the fault increases first linearly with the elastic loading up. The shear load keeps increasing up to a critical value, which corresponds to the critical strength of the fault defined by the static friction coefficient. For instance, in the case of granite, the onset of slip is observed when the friction reaches a friction coefficient of  $\approx 0.5$  (Fig. 3.2 (a.)). This phase is followed by a strengthening behaviour, i.e. an increase of the friction coefficient with cumulative slip, up a almost constant friction (steady state value) of 0.65. Once the friction coefficient presents a constant value, I imposed slip velocity steps, corresponding to instantaneous increase or decrease of the imposed velocity, to study the velocity dependence of the frictional properties of the interface (Fig. 3.2 (a.)).

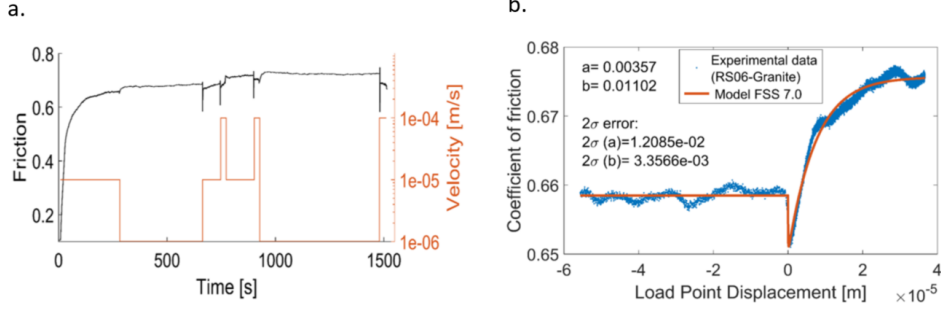


Figure 3.2: (a.) Evolution of friction with the horizontal displacement (test RS06). Seven velocity steps were imposed. (b.) Comparison between experimental data obtained during a velocity step and the results of the inversion of the rate and state parameters, conducted following the inversion code FSS 7.1 [25] (test RS06).

These velocity steps allow to estimate the rate and state parameters of the fault interface.

These parameters, commonly defined as  $a$  and  $b$  values, were first determined manually for each velocity step in the following way [35]:

$$a - b = \frac{\partial \mu^{ss}}{\partial [\ln(V)]} \quad (3.1)$$

In a second stage, the velocity steps were modelled using FSS 7.1 inversion code [25] where a slip law was imposed (Fig. 3.2 (b.)). [2] The *slip law* (Eq.3.3) differs from the *aging law* (Eq.3.2) in the way they account for the state variable behaviour. In the slip law the state variable depends on slip only, while in the aging law it evolves as well during the static stage.

$$\dot{\theta} = 1 - \frac{V\theta}{D_c} \quad (3.2)$$

$$\dot{\theta} = \frac{V\theta}{D_c} \cdot \ln\left(\frac{V\theta}{D_c}\right) \quad (3.3)$$

Six tests were analysed (RS05, RS06, RS07, RS08, RS09, RS10), focusing on the following interfaces; Granite-Granite, Gabbro-Granite, Gabbro-Gabbro.

The velocity history was kept the same for all the experiments to make possible an easy comparison between them. In particular the velocity history was (Figure 3.3):  $1e-05 \frac{m}{s}$ ,  $1e-06 \frac{m}{s}$ ,  $1e-05 \frac{m}{s}$ ,  $1e-04 \frac{m}{s}$ ,  $1e-05 \frac{m}{s}$ ,  $1e-04 \frac{m}{s}$ ,  $1e-06 \frac{m}{s}$ ,  $1e-04 \frac{m}{s}$ .

**Monomaterial interface.** The comparison between the experiments conducted on both Granite and Gabbro mono-material interfaces is presented

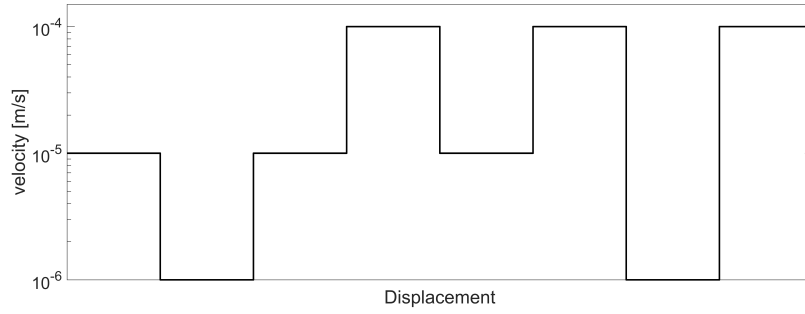


Figure 3.3: Velocity steps imposed during the test.

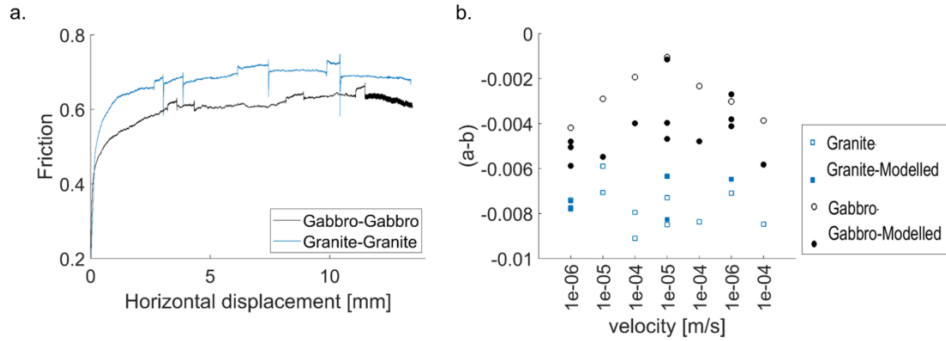


Figure 3.4: (a.) Evolution of the friction with the displacement for Gabbro and Granite (RS06, RS09). Seven velocity steps were imposed. (b.)  $(a-b)$  values computed both manually and modelled through FSS 7.1 inversion code.

in Fig. 3.4. The evolution of the two curves in Fig.3.4(a) looks qualitatively very similar. Granite reaches a value of friction higher than Gabbro of about 0.1. After a first stage of elastic loading, the friction coefficient reaches a steady-state values for both experiments. For each change of velocity a change in friction can be noticed. In particular an increase of velocity brings to a decrease in friction and vice versa [34, 14]. At each velocity step, we can measure a new steady-state friction value. The evolution of it is pretty similar and consistent for each step with the same slip rate. Note that (i) both interfaces highlight a velocity weakening behaviour ( i.e.  $a - b < 0$ ) and (ii) independently of the slip velocity,  $(a-b)$  is systematically smaller in granite (from  $-8$  to  $-14 \times 10^{-3}$ ) than in gabbro (from  $-2$  to  $-8 \times 10^{-3}$ ).

**Bimaterial interface.** After assessing the behaviour of mono-material interfaces, the influence of bi-material interfaces on rate and state parameters were investigated (Fig.3.5 test RS08). The evolution of the friction is comparable to the mono-material interface curves with values in between those

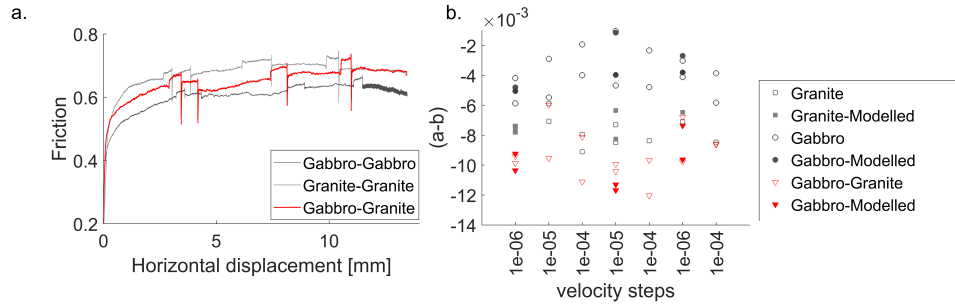


Figure 3.5: (a.) Evolution of the friction with the displacement for the bimaterial interface Gabbro-Granite (RS08). Seven velocity steps were imposed. (b.) (a-b) values computed both manually and modelled through FSS 7.1 inversion code.

of Granite and Gabbro mono-materials interfaces. Computing the rate and state values (a-b) through modelling via FSS inversion code and manually with 3.1, it can be observed that the bi-material interface shows values very similar to Granite's values (Fig. 3.4 (b.)). Moreover (a-b) seems to be controlled by Granite rather than Gabbro.

### 3.1.2 Stick-slip tests

At larger stress conditions, both stable and unstable behaviours were observed, depending on the material and the roughness applied.

All the stick-slip sequences presented here were obtained at a normal load of 1 MPa following the same velocity history; 2.5 mm at 0.10 mm/min, 1.5 mm at 0.05 mm/min, 1.5 mm at 0.1 mm/min, 1.5 mm at 0.25 mm /min , 1.5 mm at 0.50 mm /min, 1.5 mm at 0.75 mm /min. The velocities were changed to study the influence of strain-rate on stress drops recurrence and stress drops amplitude between the two materials

As we can see in Fig. 3.6 and 3.7, both Granite and Gabbro exhibits the stick-slip motions. After an initial elastic loading, the curves departs from linearity when the friction was close to its static values. At this stage, an instability occurs highlighted by a sudden release of stress induced by slip along the interface.

For each experiment a big attention was given on the stress drop of each instability. For each test, the stress drop amplitudes are plotted as a function of their related peak value of shear load.

**Effect of roughness on monomaterial interfaces.** The effect of roughness was studied to understand if one roughness or the other was able to control the behaviour of the *bi-roughness* sample. To study this effect of roughness, we conducted the following tests;  $Gab_{rough} - Gab_{rough}$ ,  $Gra_{rough} -$

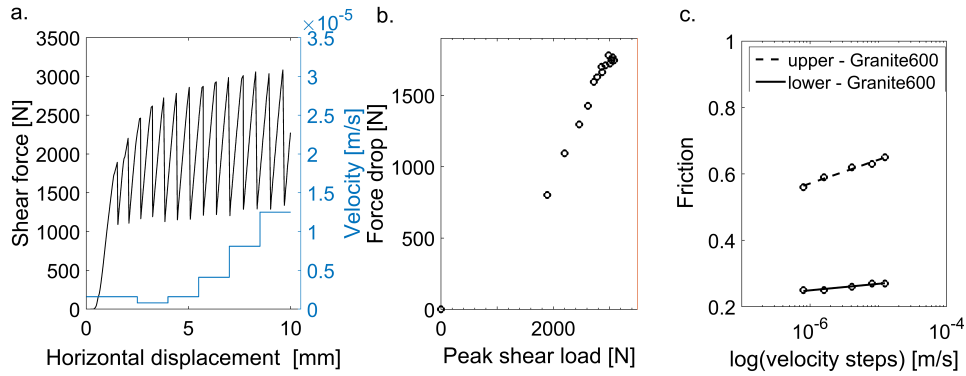


Figure 3.6: (a.) Unstable behaviour of Granite (grid 600) (Stick slip). (b.) Force drops vs peak shear load reached by each single drop. (c.) Evolution of friction with the logarithm of the sliding velocity.

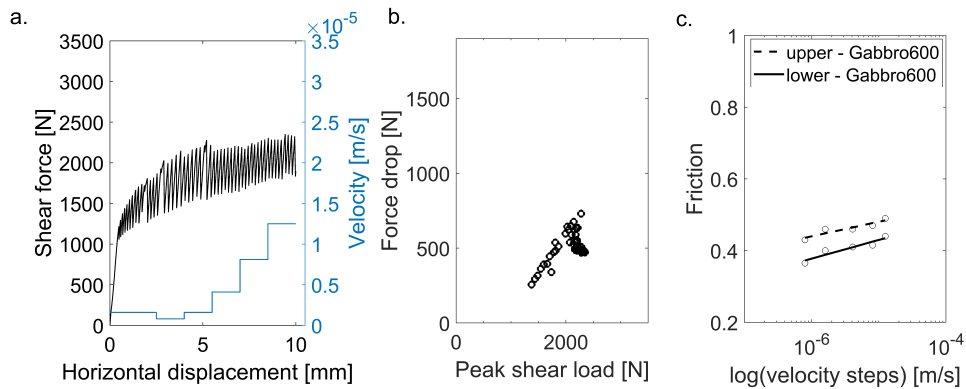


Figure 3.7: (a.) Stick-slip sequence observed during an experiment on  $Gab_{smooth}$ . (b.) Force drops vs peak shear load reached at each single event. (c.) Evolution of friction with the logarithm of the sliding velocity.

$Gra_{rough}$ ,  $Gab_{smooth}$ - $Gab_{smooth}$  and  $Gra_{smooth}$ - $Gra_{smooth}$ . In a second stage, we combined the two different roughness along a single interface composed of the same material, resulting in the experiments  $Gab_{rough}$ - $Gab_{smooth}$ ,  $Gra_{rough}$ - $Gra_{smooth}$ .

In the case of gabbro, the rough interface exhibits stable behaviour also at high normal load conditions (1MPa). In contrary, decreasing the roughness allows the transition from stable to unstable behaviour. In such case, the force drop increases with increasing the peak shear load. Remarkably, combining both roughness along a same interface, the resulting fault exhibits stable slip behaviour (Figs. 3.9 a and b). This result suggests that in the case of Gabbro, the frictional behaviour is controlled by the rougher interface, which exhibits systematically stable slip behaviour.

In contrast with Gabbro, Granite interface always exhibits unstable behaviour and stick-slip events under 1MPa normal stress conditions, regardless the roughness imposed. However, both peak strength of the fault and stress drops change with the roughness of the interface. The larger the roughness of the interface is, the larger the peak shear strength of the interface (mostly in the first millimetres of slip). However, stick-slip events recorded during the experiment conducted on rough interface present smaller stress drops than events recorded on the smooth interface for equivalent peak shear load (Figs. 3.9 c and d). Combining both roughness's along a simple interface ( $Gra_{rough}$ - $Gra_{smooth}$ ) results also in unstable behaviour. In this case, the stick-slip events present an average stress drop in between events observed on rough interface and events observed on smooth interface. These results suggest that the roughness controls both the accumulation and the release of strain during the stick cycle, as well as the frictional behaviour of the interface.

One can notice how, for both materials (Gabbro and Granite), the smoother the surface of the fault, the larger the resulting stress drop at a given shear load. For what concerns granite we can see that for the rougher fault the force drops are quite small while the smoother one induces clearly bigger force drops.

**Effect of bimaterial.** To study the effect of bi-material interface, two more experiments were run, with faults that have on one side Gabbro and on the other side Granite, for both roughness's (Grid60 and Grid600). Depending on the roughness, two different effects can be observed. Grid60  $Gra_{rough}$ - $Gab_{rough}$  behaviour is controlled by Gabbro. As we can see in 3.9, both  $Gab_{rough}$  and  $Gra_{rough}$ - $Gab_{rough}$  show stable sliding. This reveals that, for these two specific kinds of material, given  $Gab_{rough}$  showing systematically a stable behaviour, then the bi-material interface will show as well a stable behaviour even if  $Gra_{rough}$  has shown stick slips at the same conditions.

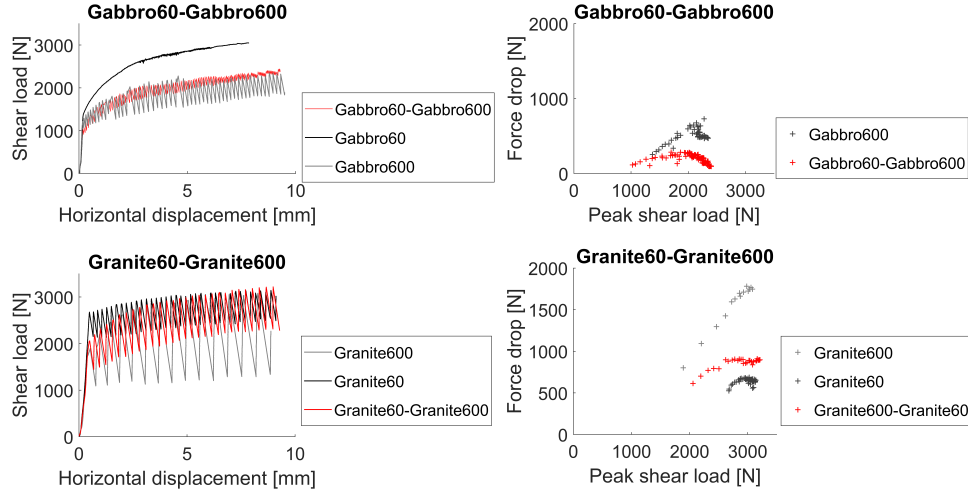


Figure 3.8: Effect of roughness on monomaterial interface.

Although at a much lower roughness (grid600)  $\text{Gra}_{rough}\text{-Gab}_{rough}$  behaviour looks to be controlled by both materials properties, resulting in force drops corresponding to an average between values observed on smoothed interface for equivalent roughness. We can see in 3.9 that the peak shear loads are quite high, as well for Granite and the force drops also present an amplitude which is still in between the other two configurations but closer to Granite's. To prevent from side effects during the experiment, due to the setup of the sample, for the mixed combination Gabbro-Granite at grid600, two different tests were carried out. In  $\text{Gra}_{smooth}\text{-Gab}_{smooth}$  the side with Gabbro was put on the bottom while the side with Granite was put on top. In the same way another experiments was conducted where Granite was at the bottom while Gabbro was on the top. Despite the initial part of the loading ramp, the results show a very similar behaviour, demonstrating that there is no side effect due to the machine configuration.

**Combination of bimaterial and biroughness effects.** Finally other two tests were carried out, to study the mixed influence caused by both different materials and different roughness. The two experiments are:  $\text{Gab}_{rough}\text{-Gra}_{smooth}$  and  $\text{Gab}_{smooth}\text{-Gra}_{rough}$ .

$\text{Gab}_{rough}\text{-Gra}_{smooth}$ , as can be seen in Fig.3.10, shows a behaviour that seems quite in the middle of the two others, even if the maximum shear load remains a bit smaller. It is important to underline that in this case the behaviour of the bi-material interface is not controlled by  $\text{gab}_{rough}$ . Indeed, contrary to gabbro behaviour, the bi-material interface showed unstable behavior.

For what concerns  $\text{Gab}_{smooth}\text{-Gra}_{rough}$ , Fig.3.10, the behaviour is not

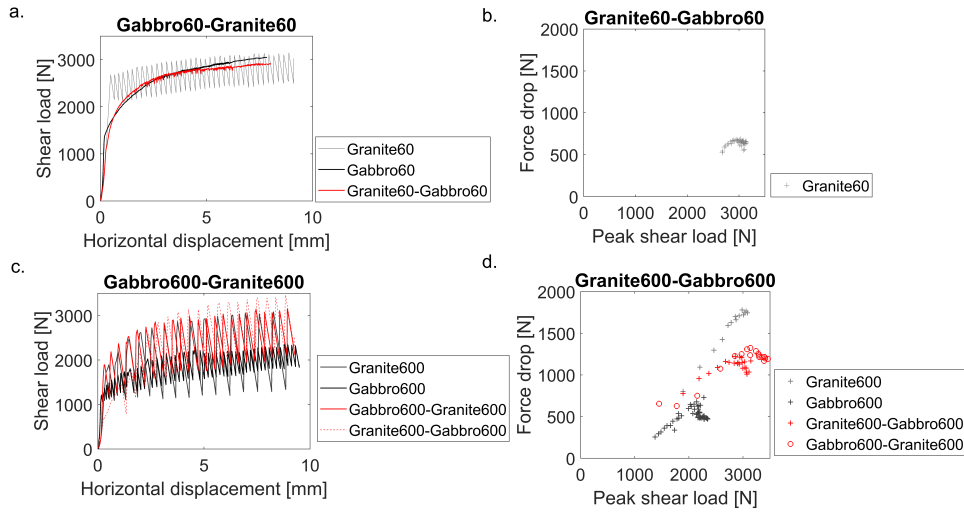


Figure 3.9: Effect of bimaterial.

very clear since it seems independent on the two related standard configurations ( $Gab_{smooth}$  and  $Gr_{rough}$ ). Only the stress drops amplitude shows a link with  $Gab_{smooth}$  and  $Gr_{rough}$  while the peak stress is much lower.

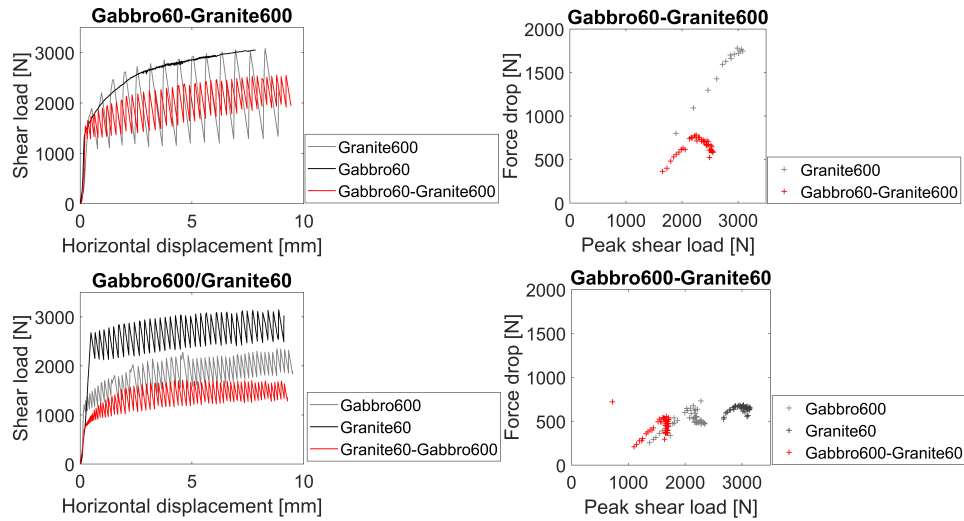


Figure 3.10: Combination of bimaterial and biroughness effects.

All the results are summarized in Tab. 3.1.

**Description of stick-slip phenomenon.** The physical phenomenon of stick-slip can be explained thanks to the equations of motion. This para-

Experiment	Behaviour
$Gab_{rough} - Gab_{rough}$	stable
$Gra_{rough} - Gra_{rough}$	unstable
$Gab_{smooth} - Gab_{smooth}$	unstable
$Gra_{smooth} - Gra_{smooth}$	unstable
$Gab_{rough} - Gab_{smooth}$	unstable
$Gab_{rough} - Gra_{rough}$	stable
$Gab_{smooth} - Gra_{smooth}$	unstable
$Gab_{rough} - Gra_{smooth}$	unstable
$Gab_{smooth} - Gra_{rough}$	unstable

Table 3.1: Table summarizing all the experiments done with Stressentest at an applied normal load of 1 MPa.

graph I will refer to what carefully explained in [17] and the same model of the mechanical system producing stick-slip behaviour will be used.

Observing the scheme in Figure 3.11 we can see that we have a system composed by a block of mass  $m$  attached to a spring of elastic constant  $k$ . The edge of the spring is pushed with a velocity  $v$ .

In a first phase the block will remain still because of the resisting frictional

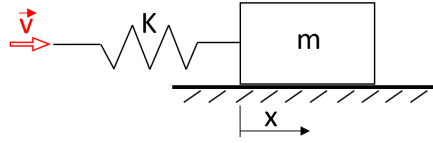


Figure 3.11: Scheme of the mechanical system spring-block.

force. The elastic force generated by the spring is given by:

$$F_{el} = K(vt - x) \quad (3.4)$$

where  $vt$  is the changing position of the edge of the spring and  $x$  is the position of the block. For sake of simplicity we will use a new time variable which will start counting time from when the block starts moving.

$$\tau = t - t^* \quad (3.5)$$

Eq. 3.4 will then turn into:

$$F_{el} = K(v\tau + vt^* - x) \quad (3.6)$$

The mass will start moving only when the elastic force will equal the frictional force. We will call the time at which the block starts moving  $t^*$ .

Considering the block at the initial position  $x=0$  then:

$$F_{el} = Kvt^* = \mu mg = T_s \quad (3.7)$$

From 3.7 we can observe the following relationship:

$$vt^* = \mu \frac{mg}{K} \quad (3.8)$$

For  $t > t^*$  the motion of the block will be obstructed by the dynamic frictional force  $T_d = -\mu_d mg$ .

The equation of motion can then be written as follows:

$$m\ddot{x} = k(v\tau + vt^* - x) - \mu_d mg \quad (3.9)$$

The initial conditions to solve this differential equation are:

$$t = t^* \rightarrow \tau = 0 \quad (3.10)$$

$$x = 0$$

$$\dot{x} = 0$$

By applying now a change of variables we can use a new variable to describe the position of the system:

$$p = v\tau + vt^* - x - \mu_d \frac{mg}{K} = v\tau - x + (\mu - \mu_d) \frac{mg}{K} \quad (3.11)$$

by using 3.7. The adjusted initial conditions are:

$$t = t^* \rightarrow \tau = 0 \quad (3.12)$$

$$p = (\mu - \mu_d) \frac{mg}{K}$$

$$\dot{p} = v$$

The solution of this equation is written in the following way:

$$p = A \sin(\omega t) + B \cos(\omega t) \quad (3.13)$$

By replacing the initial conditions it can be written:

$$A = \frac{v}{\omega}$$

$$B = (\mu - \mu_d) \frac{mg}{K}$$

The solution then is:

$$p = \frac{v}{\omega} \sin(\omega t) + (\mu - \mu_d) \frac{mg}{K} \cos(\omega t) \quad (3.14)$$

Since we are still interested in the position of the block, we can rewrite 3.14 as follows:

$$x = v\tau + (\mu - \mu_d)\frac{mg}{K} - \frac{v}{\omega}\text{sen}(\omega t) - (\mu - \mu_d)\frac{mg}{K}\cos(\omega t)$$

Replacing  $\frac{K}{m} = \omega^2$ , which is the square undamped natural frequency of the system we can rewrite:

$$x = v\tau + (\mu - \mu_d)\frac{g}{\omega^2} - \frac{v}{\omega}\text{sen}(\omega t) - (\mu - \mu_d)\frac{g}{\omega^2}\cos(\omega t) \quad (3.15)$$

$$\dot{x} = v - v\cos(\omega t) + (\mu - \mu_d)\frac{g}{\omega}\text{sen}(\omega t) \quad (3.16)$$

Equation 3.15 describes the motion of the block while equation 3.16 describes its velocity. Once the block will start moving, we will have a first phase of slip followed by a phase of stick. During the stick phase the block is still and  $\dot{x} = 0$ . By inverting this last relationship we can get the duration time of the slip phase:

$$\tau_{slip} = \frac{2}{\omega} \left( \pi - \tan^{-1}\left((\mu - \mu_d)\frac{g}{v\omega}\right) \right) \quad (3.17)$$

With the latter we can then write the displacement of the block during the slip phase:

$$x_{slip} = v\tau_{slip} + 2(\mu - \mu_d)\frac{g}{\omega^2} \quad (3.18)$$

The minimum elastic force can be written as can be found in ??as:

$$T_{slip} = (2\mu_d - \mu)mg \quad (3.19)$$

which means that the following relationship can be used:

$$2\mu_d - \mu_{up} = \mu_{low} \quad (3.20)$$

The spring will now stay still for a certain amount of time, until the elastic force reaches again the static frictional value.

$$\tau_{stick} = 2(\mu - \mu_d)\frac{g}{v\omega} \quad (3.21)$$

Combining equation 3.17 and equation 3.21 we can define the duration time of an entire cycle:

$$\Delta\tau = \tau_{slip} + \tau_{stick} \quad (3.22)$$

**Friction evolution.** As well explained in [17] and as showed also in the last paragraph, during stick-slip tests both maxima and minima peaks of the shear force reach a plateaux.

By dividing the shear load values by the normal load (which was kept constant during the test) it was possible to obtain the evolution of friction during the experiments. Once located the plateaux, the friction coefficient was extracted. For the tests that showed stick-slip, two plateaux could be defined and so two friction coefficients. As it is intuitive to think, smoother surfaces show a lower friction coefficient than rougher ones.

As well explained in [17] two friction values show up in stick-slip tests;  $\mu_{up}$  and  $\mu_{low}$ . Since  $\mu_{up}$  refers to the shear force in the moment right before the slip occurs, then that specific friction value can be recognized as the static friction value. In [17]  $\mu_{up}$  and  $\mu_{low}$  are linked together by 3.20.

The latter comes, as it was showed in the last paragraph, from a force balance in the modelling of stick-slip through a spring-mass mechanical system. Then referring to this equation it is possible to obtain the dynamic friction coefficient as follows:

$$\mu_d = (\mu_{up} + \mu_{low})/2 \quad (3.23)$$

and the static friction coefficient as stated before will be given by:

$$\mu_s = \mu_{up} \quad (3.24)$$

Another significant aspect that can be noticed from these results is how friction changes also depending on the slip rate. This is more accentuated and evident for Gabbro than for Granite, even if in both cases we have a change in values as we go through different slip velocities. Moreover as we pass to higher slip velocities the drops seem to be smaller than the previous ones and the recurrence time shorter as well. This aspect, as well, can be noted much more in Gabbro than in Granite. Moreover, since these tests were run changing slip velocity each 1.5 mm displacement it was also possible to verify that the dynamic friction coefficient changed depending on the logarithm of the slip rate (as already known from Rate and state theory).

## 3.2 Discussion.

Frictional resistance between surfaces has long been investigated in the past centuries. In 1699, Amantons observed that the macroscopic friction on an interface does not depend on the microscopic area of contact and it only depends on the applied load. In the last century, Bowden and Tabor (1938) first investigated the role of the real area of contact. Their analysis shows that friction is proportional to the real area of contact between two surfaces,

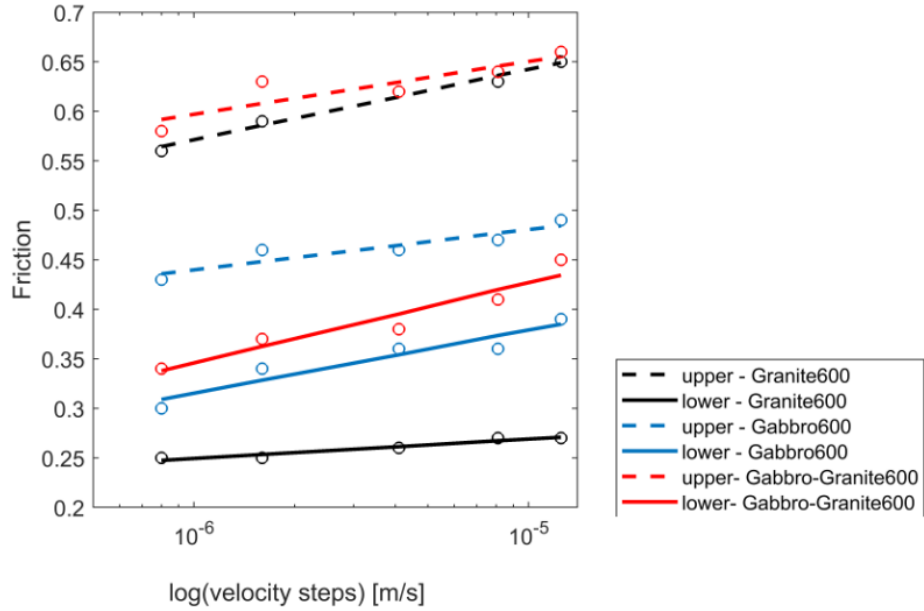


Figure 3.12: Evolution of upper and lower values of friction.

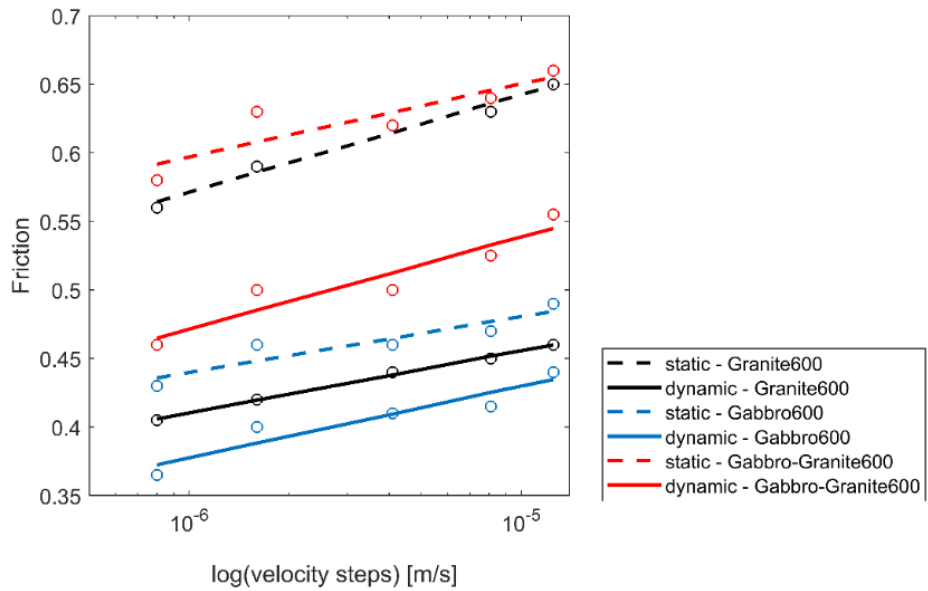


Figure 3.13: Evolution of static and dynamic values of friction.

that derives from the asperity contacts constituting the roughness of the surface. Following their observations, friction depends on both the real contact area and the capability of the asperities to undergo plastic deformation. Several studies have focused on the role of roughness on surface friction [6, 7]. These studies show that the friction of the interface is controlled by the roughness. However, only few studies have been conducted to investigate the effect of roughness on fault frictional stability that is still poorly understood. In this thesis, it was investigated the effect of different roughness and different lithology on fault slip behaviour, as well as the effect of asymmetric roughness and bi-material interface. In the following, the main findings are summarized and discussed .

- The mechanical data show that an increase in normal load favours unstable slip behaviour. These results agree with the rate and state theory. Indeed, equation 1.4 predicts that an increase in normal stress increases  $K_C$ , thus favouring the transition from slow and stable sliding to unstable slip (i.e., earthquakes), if the  $K_C$  exceeded the stiffness of the machine;
- At lower normal stress, under stable sliding conditions, Gabbro and Granite show different values of friction coefficient. The Gabbro has systematically lower friction values. Moreover, both the materials are characterized by velocity-weakening behaviour, that is negative (a-b) values (Fig.3.4). Granite, with more negative (a-b) values is more velocity-weakening and thus more prone to slip unstably than Gabbro, which has higher values. Coherently, at higher normal stress, Gabbro is characterized by lower peak friction values. In particular, at low roughness (P600), the peak friction value of Granite is 0.65, while the peak friction value of Gabbro is 0.55 (Fig.3.8). The overall higher values of force drops of Granite with respect to Gabbro is in good agreement with the more negative (a-b) values and the more unstable behaviour characterizing the Granite;
- The roughness plays an important role in controlling the fault stability. We observe that changing the roughness of the sample, the stability systematically changes (Fig.3.8). At the same boundary conditions (normal load, slip velocity), at a high roughness (P60) Gabbro shows a stable behaviour, while with a low roughness (P600) it shows an unstable behaviour. A similar trend can be observed in the Granite. Even if in both roughnesses it shows unstable behaviour, the amplitude of the force drops is indeed higher for smoother surfaces and lower for rougher surfaces, suggesting a more unstable behaviour for low roughness (P600). This can be theoretically explained by Eq. 1.4, inferring that  $D_c$  changes as a function of roughness. Indeed it has

been experimentally showed [29, 13], that an increase of roughness results in an increase in  $D_c$  value. Consequently, a  $D_c$  increases results in decreasing the critical stiffness, thus favouring stable sliding;

- For asymmetric roughness interfaces the resulting behaviour shows in an intermediate between the two roughness (Fig.3.8).
- For bi-material interface the overall behaviour is an average of the two mono-materials (Fig.3.9). Specifically, we distinguish between stable sliding experiments and unstable experiments. Again, the increase in normal load results in the transition from stable sliding to mainly unstable sliding behaviour, accordingly to equation 1.4. At a low normal load (0.15 MPa), the bi-material interface shows a friction value which is an average of the two mono-material behaviours. The (a-b) values of the bi-material interface are partially overlapping to Granite values (slightly more negative). At a high normal load (1MPa), for the higher roughness (P60) the bi-material shows a stable behaviour strongly controlled by Gabbro, while for the lower roughness (P600) it shows an unstable behaviour characterized by force drops values that are intermediate with respect to the mono-materials and nearer the values of Granite.
- Overall, the roughness seems to play a key role in controlling the fault stability.

## Chapter 4

# Propagation of rupture. Hopkinson 2D

Shear apparatus similar to the Hopkinson 2D are commonly used to investigate the frictional motion at the onset of dynamic rupture [5, 4, 41, 39, 38]. The advantage of these apparatus is mostly the size of the sample, which allows the monitoring of strain and stress at various locations along the fault. However, most of the experimental studies using this experimental set-up focused on synthetic and analogue materials, such as PMMA or gel and very few of them were conducted on rocks. A large part of this thesis consists in the development and the calibration of the shear Hopkinson apparatus configuration. While more than 70 experiments were conducted during the stage, here are presented the results of the three last experiments, which correspond to the final experimental configuration. The evolution of stress was monitored using two load cells which allow the measurement of the macroscopic loads (normal and shear) applied on the two blocks during experiments. In addition, 7 rosettes composed of three individual strain gauges were used to measure the complete strain tensor at seven different locations along the fault strike direction. Finally, 11 acoustic sensors were glued on the moving sample in front to the strain gages to record acoustic emissions.

### 4.1 Experimental results

Among all the experiments, the following three were selected to be presented here (Gabbro-Gabbro, Fig. 4.1a), (Granite-Granite, Fig. 4.1b), (Gabbro-Granite, Fig. 4.1c).

First of all, the normal load was increased to a target value. Then, it was servo controlled to remain constant using a pressure regulator system. The shear load was applied manually up to a final shear displacement of 3 centimeters. The evolution of the normal load, of the shear load and of the

acoustic emissions rate are presented in figure 4.1 (AE rate was not estimated for experiments conducted on granite).

For each experiment, the onset of acoustic emissions activity occurred at the initiation of the shear loading. Shear load increases continuously up to value close to the peak strength of the fault. At this stage, granite interface exhibited small events releasing partially the macroscopic shear load. The amplitude of the events increases with the loading, up to the onset of a big and strong instability, releasing almost the entire stress accumulated along the fault interface. Mostly large macroscopic events occurred during experiments conducted on gabbro and on bimaterial interface.

## 4.2 Estimation of local strain and stress along the fault plane

**Strain and stress components** Rosettes strain gauges were used to compute the complete strain and stress tensors at different positions along the fault. Following the experimental configuration, the strain tensor components are related to the direct measurement following (see Appendix B for demonstration):

$$\varepsilon_{yy} = \varepsilon_1 \quad (4.1)$$

$$\varepsilon_{xx} = \varepsilon_3 + \varepsilon_2 - \varepsilon_1 \quad (4.2)$$

$$\varepsilon_{xy} = \varepsilon_3 - \varepsilon_2 \quad (4.3)$$

The stresses  $\sigma_{yy}, \sigma_{xx}, \sigma_{xy}$  are computed from the strain tensor assuming the hypothesis of plane stress conditions, which is reasonable since the thickness of both blocks is quite smaller compared to their dimensions along x and y axis (almost one order of magnitude). Assuming this, stresses are related to strain following:

$$\sigma_{yy} = \frac{E}{(1 + \nu)^2} (\varepsilon_{yy} + \nu \varepsilon_{xx}) \quad (4.4)$$

$$\sigma_{xx} = \frac{E}{(1 + \nu)^2} (\varepsilon_{xx} + \nu \varepsilon_{yy}) \quad (4.5)$$

$$\sigma_{xy} = \frac{E}{2(1 + \nu)} \varepsilon_{xy} \quad (4.6)$$

Despite the strain gages are located at 3-5 mm from the fault plane, measurements can be corrected to estimate the stress on the fault plane, in which we are mostly interested. The stress on the fault [4] ( $\sigma_{xy}$  in ( $y = 0$ )) is estimated assuming a tangent approximation within the first degree Taylor expansion of  $\sigma_{xy}$  following (see Appendix B for details):

$$\sigma_{xy\text{corrected}} = \sigma_{xy} - \Delta y \frac{\partial \sigma_{xy}}{\partial y} \quad (4.7)$$

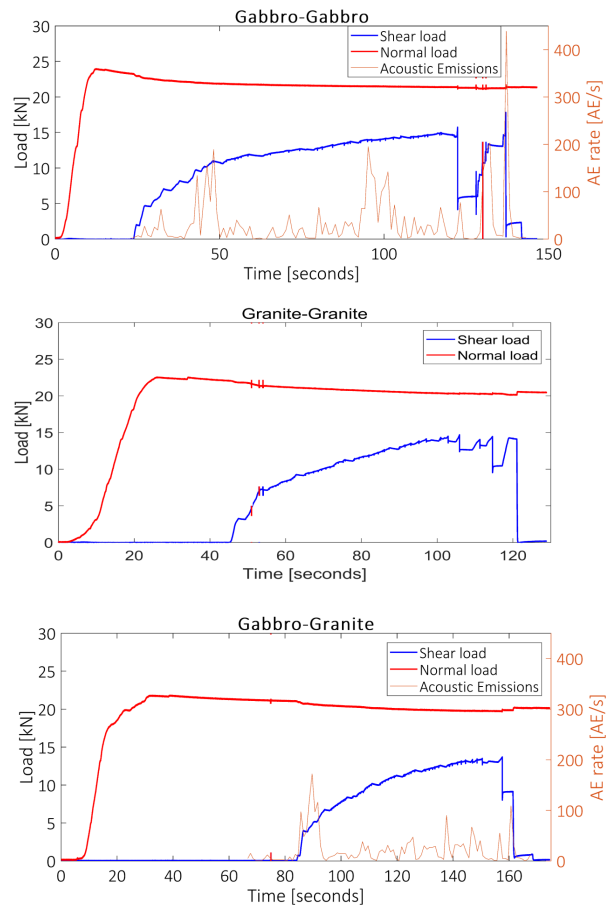


Figure 4.1: Mechanical results of the two applied loads; normal load and shear load. Evolution of the acoustic emissions with time. Are reported the three experiments: T10 (Gabbro-Gabbro), T13 (Granite-Granite), T12 (Gabbro-Granite).

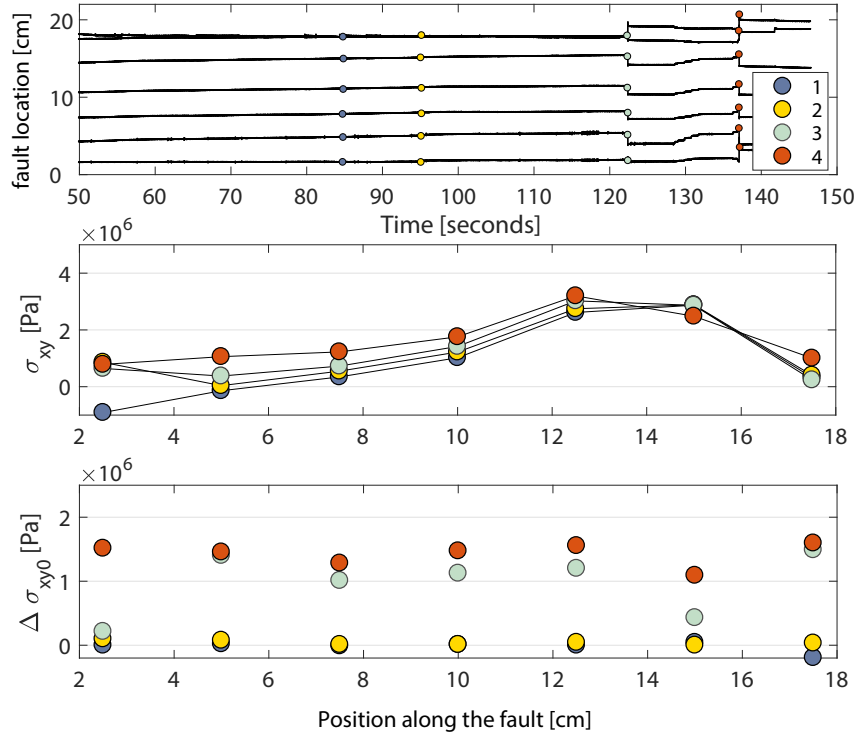


Figure 4.2: Evolution of stress along the fault test T10.

To get the derivative term we can use stress equilibrium in x direction for which:

$$\sigma_{xy} + \frac{\partial \sigma_{xy}}{\partial y} dy + \sigma_{xx} + \frac{\partial \sigma_{xx}}{\partial x} dx - \sigma_{xy} - \sigma_{xx} = 0 \quad (4.8)$$

$$\frac{\partial \sigma_{xy}}{\partial y} dy + \frac{\partial \sigma_{xx}}{\partial x} dx = 0 \quad (4.9)$$

Equation 4.7 will then be:

$$\sigma_{xy}^{y=0} = \sigma_{xy} + \Delta y \frac{\partial \sigma_{xx}}{\partial x} \quad (4.10)$$

In the following,  $\sigma_{xy}$  will always refer to the corrected stress  $\sigma_{xy}^{y=0}$ .

The evolutions of  $\sigma_{xy}^{y=0}$  at the different locations along the fault during the experiment conducted on Gabbro are presented in Figure 4.2a. Each stress curves were normalized by their maximum values. Note that the shear stress evolves in a similar way all along the fault, expected at the two edges of the fault due to the block edges effect[5]. This behaviour is due to dilation induced by the loading point on the loaded side, and by the stopper on the other side of the fault. The latter can bring non-uniformity due to stresses concentrations which may be higher than the distributed

stress along the fault, affecting the stress profile itself. However the strain gages located in the central part of the fault allow to estimate the stress distribution before minor or strong instabilities, as well as the stress drop due to finite or macroscopic ruptures of the interface.

**Stress distribution.** Figure 4.2b presents the stress distribution along the fault prior four different events. The stress distribution before each event is comparable despite the cumulative slip. Note that the right sample edge presents negative values of stress prior the first events, probably due to the edge effects explained previously. However, the stress distribution is positive within the central part of fault. Before each event, the maximum stress is observed at the location  $x=12.5$  cm, with values ranging from  $\sigma_{xy}^{y=0}$  2.7 to 3.2 MPa. Cumulative events seem to increase the initial stress on the left side of the fault (from 0 to 1.3 MPa at  $x=5$  cm prior event 1 and 4, respectively), while the stress remains very comparable on the right side, i.e. close to the loading point (Figure 4.2b). The cumulative loading, i.e. the cumulative number of events, seems to homogenize the stress distribution along the fault and the stress is positive in between 1.2 and 3MPa along the fault prior the last events.

**Stress drop and stress transfer during rupture phenomena** The two first events were recorded during the first part of the experiments and did not induce a macroscopic stress release (Figure 4.1a). The two last events presented here induced a strong macroscopic release of stress, recorded also on the shear load cell (Figure 4.1a). Using the strain gauges measurements,  $\Delta\sigma$  was obtained by subtracting the residual stress after a drop to the initial stress distribution, at each location of the strain gages.

The first two events released a small amount of stress compared to the stress distribution profile. During these first events, a release of stress is mostly observed between the position  $x=4$  cm and  $x=16$ . Conversely, a stress accumulation is observed at the edge of the sample, suggesting that rupture did not reached the sample edge, explaining the small amount of the stress release. The last two events released a larger amount of stress, ranging from 0.3 to 1.8 MPa. The biggest drops are observed for the last events, which also presented the largest initial stress profile. Note that the stress drop does not seem to depend on the initial stress.

### 4.3 Analysis of acoustic data

**Acoustic emission activity** For each acoustic emission recorded during stick-slip cycles, the first wave arrival recorded on each sensor during each event was automatically picked using RMS function provided by Insight software (the accuracy of picking is in the order of  $0.01 \mu s$ ). To estimate the

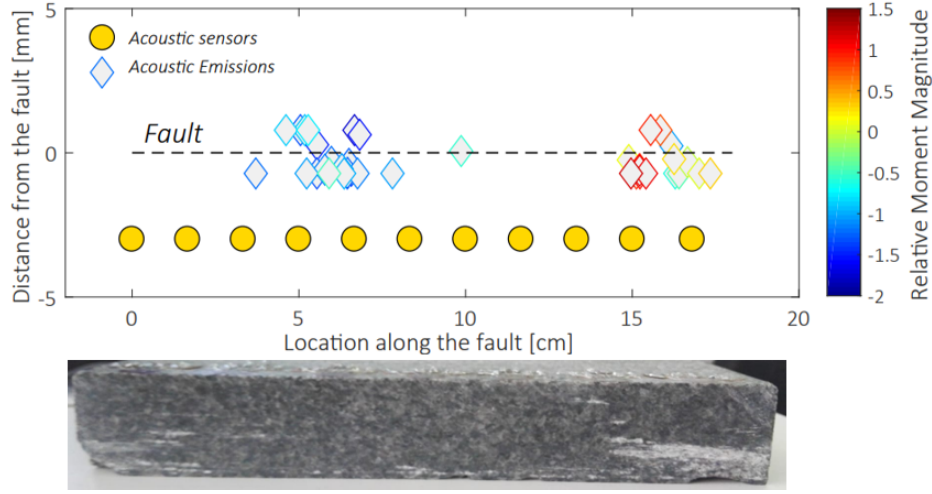


Figure 4.3: Location of AEs during experiments.

location of each AE, the first step consists of the calculation of the theoretical travel time between a nucleation point  $(X, Z)$  around the fault plane and the piezoelectric sensor array locations  $(X_k, Z_k)$ . We assume here a 3D geometry of the fault plane with a fault thickness of 1cm which corresponds to the size of the largest crack observed on the post-mortem samples. The theoretical travel times can be calculated by the expression:

$$t_{(i,k)} = \frac{\sqrt{(X - X_k)^2 - (Z - Z_k)^2}}{C_P} \quad (4.11)$$

where  $C_P$  is the compressional wave velocity and  $i$  the number of the event. Time residuals are calculated between experimental arrival times ( $t^{exp}$ ) and the theoretical ones for different rupture initiation times ( $t_0$ ) following

$$\Delta t(C_P, k, t_0) = \sqrt{\frac{\sum_0^k |t_{(i,k)}^{exp} - t_{(i,k)} - t_{0(i)}|}{n}} \quad (4.12)$$

The sum of the residual time for each sensor is then computed for one nucleation point and one initiation time using a least-square function and then computed for each location  $(X, Z)$  of the fault plane and for different initiation times. A simple least square minimisation outputs the nucleation point of the event and its time of initiation. The average value of the residual time for all AEs located is about  $0.1 \mu s$ , corresponding to location accuracy of  $0.5 \text{ mm}$  assuming  $C_P=4950 \text{ m/s}$ . This method allows the removed of AEs nucleating far away from the fault by neglecting all AEs presenting a residual time higher than  $0.2 \mu s$  (i.e., outside of the fault thickness considered here).

Note however that more than 95 % of the AeS are located into the considered fault thickness.

The distribution of the hypocenters corresponding to the biggest AEs recorded during the experiment conducted on bi-material interface is presented in Figure 4.3. Two main clusters are observed. The first cluster is located at  $x=5$  cm, and the second is located at the position  $x=16$  cm (Figure 4.3a). Note that the average magnitude of AEs is a function of the position along the fault. Relative magnitude of AEs ranges from -2 to -0.7 within the first cluster, while AEs nucleating within the second cluster present relative magnitude ranging from -0.9 to 1.5 (Figure 4.3a). Comparing our location results to a picture of the post mortem fault surface highlights that the second cluster, presenting the strongest AEs, corresponds to an area where strong striation and damage are observed. Note that the largest AEs occurred where the stress is maximum prior large event.

**Rupture velocity** The unsaturated waveforms recorded using the digital oscilloscope can be used to estimate the rupture velocity corresponding to macroscopic events. As stated previously, acoustic transducers located along the fault preferentially recorded the passage of the rupture front during large events. In such case, the rupture corresponds to the first wave arrival on each sensors.

In particular the arrival front was picked manually using the graphical output of Insight Software. Since all the waveforms resulted sufficiently neat, it was easy to estimate the arrival of the rupture wave front. For each experiment four big events were selected. Afterwards each event was analysed and for each acoustic sensor the arrival was chosen looking at the acoustic waves. By connecting all the points representing the rupture arrival, it was possible to estimate the rupture front of the specific event (Figure 4.4,4.5,4.6).

Knowing the location of each sensors,  $V_r$  (rupture velocity) corresponds to the distance between each transducer divided by the time difference of the first wave arrival.  $V_r$  was calculated for four large events recorded during each experiments. In each of these cases, rupture velocity is faster than the S wave speed of the related material (shown in Tab. 2.3).

For all the three tests the rupture velocity was quite consistent for each event. For example in test T10 (Gabbro-Gabbro) the estimated rupture is in the range between 6000 and 6300 m/s. In test T13 (Granite-Granite) the estimated rupture is in the range between 4900 and 5300 m/s. In test T12 (Gabbro-Granite) the estimated rupture is in the range between 4500 and 5300 m/s. These values are showed in figure 4.7. For each plot the P wave velocity and the S wave velocity are showed through dashed lines. Note that for test T10 (4.7 a.) and T13 (4.7 b.) the rupture velocity is slightly lower than P wave velocity of respectively Gabbro and Granite. For the

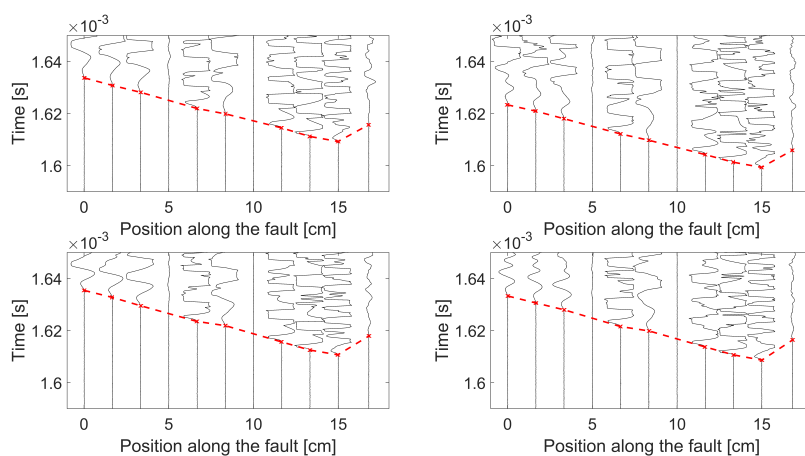


Figure 4.4: T10, Gabbro-Gabbro. Acoustic waveform along the fault for four events. In red rupture propagation.

bi-material interface, test T12, the rupture velocity is in between  $V_P$  and  $V_S$  of Granite.

In all the experiments the rupture velocity turns out to be supershear velocity.

## 4.4 Interpretation and discussion

### 4.4.1 Comparison between stress distribution and rupture nucleation

Another analysis was done by comparing at the same time the mechanical and the acoustic results. For each test, a big event was selected and the results obtained from the acoustic data and from the mechanical data were studied (Fig. 4.8, 4.9, 4.10).

For each experiment we can observe three sub plots. In plot a. the waveforms are showed, for each acoustic sensor. In fact in the x-axis is represented the position along the fault while in the y-axis is represented the relative time at which the event occurred. In plot b. the stress distribution along the fault is showed, for each strain gage position. In fact in the x-axis is represented the position along the fault while in the y-axis is represented the stress estimated right before the event occurred. In plot c. the stress drops distribution is showed, for each strain gage position. In the x-axis is represented the position along the fault while in the y-axis is represented the stress drop characterizing the event. In general, by looking at the three tests, we could say that the rupture seems always to nucleate where there is a higher concentration of stress along the fault. By looking at the sub plots a. and b. it is easy to notice that the nucleation point coincides with

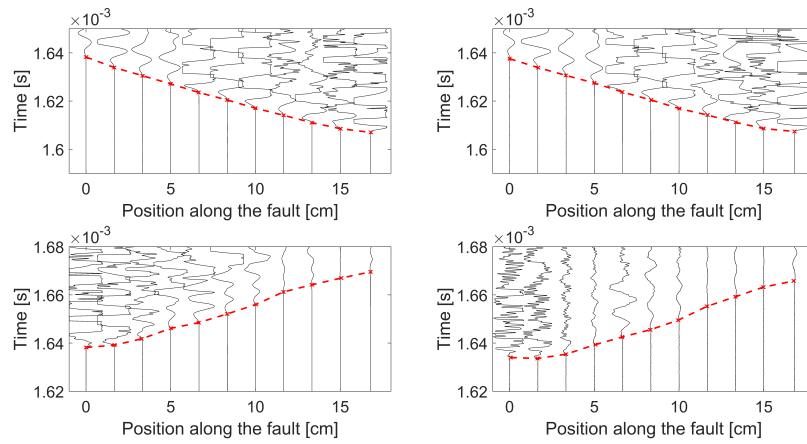


Figure 4.5: T13, Granite-Granite. Acoustic waveform along the fault for four events. In red rupture propagation.

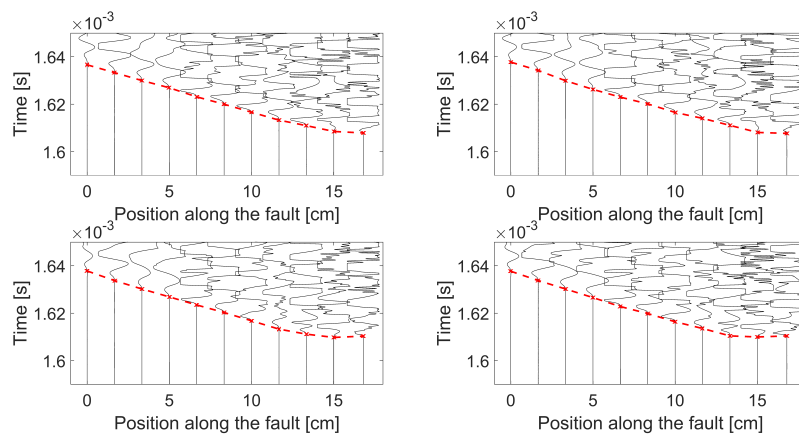


Figure 4.6: T12, Gabbro-Granite. Acoustic waveform along the fault for four events. In red rupture propagation.

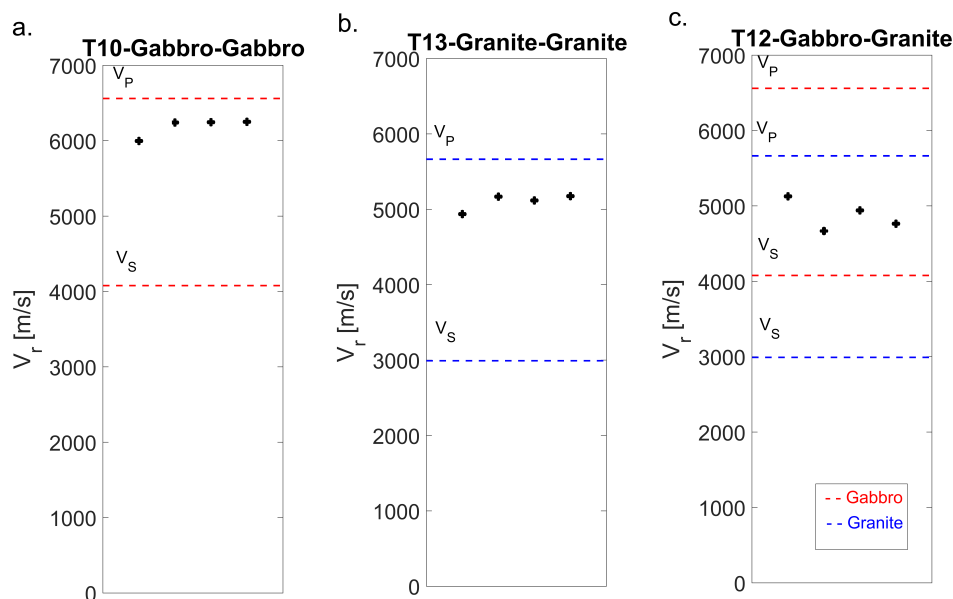


Figure 4.7: Rupture propagation velocity for T10, T13, T12.

the maximum of the absolute value of the stress distribution. For test T10 (Figure 4.8) the nucleation occurs on the right side of the fault, just where the stress is of about  $3 \times 10^6 \text{ Pa}$ , the maximum value. For test T13 (Figure 4.9) the nucleation occurs on the left side of the fault, just where the stress is as well of about  $3 \times 10^6 \text{ Pa}$ , the maximum value. For test T10 (Figure 4.10) the nucleation occurs on the right side of the fault, just where the stress is of about  $2.5 \times 10^6 \text{ Pa}$ , the maximum value.

Moreover the sign of the computed stress drops should suggest us either if the rupture is propagating (releasing stress which we can recognize in a positive stress drop) or if it is arresting (local increase of stress which can be recognized in a negative stress drop). For test T10 (Figure 4.8) it was just pointed out that the nucleation occurred on the right side of the interface. In plot c. we can see how on the left of the nucleation point all the stress drops are positive, meaning that the rupture is propagating through. On the right of the nucleation point, the stress drop is negative, meaning that the rupture is arresting. This can also be the reason why the slope of the rupture front in plot a. is higher than the propagating front. In test T13 the rupture nucleated on the left and propagated through the interface arresting right after the mid distance where the stress drops turn negative. In plot a. it can be noticed that there is almost no wave signal corresponding to the location at which the rupture starts to arrest. In test T12 the stress drops are positive for the whole extension of the interface; this means that from the right edge of the fault, the rupture propagates until the end.

In experiment T10 we can clearly notice how the rupture nucleates at

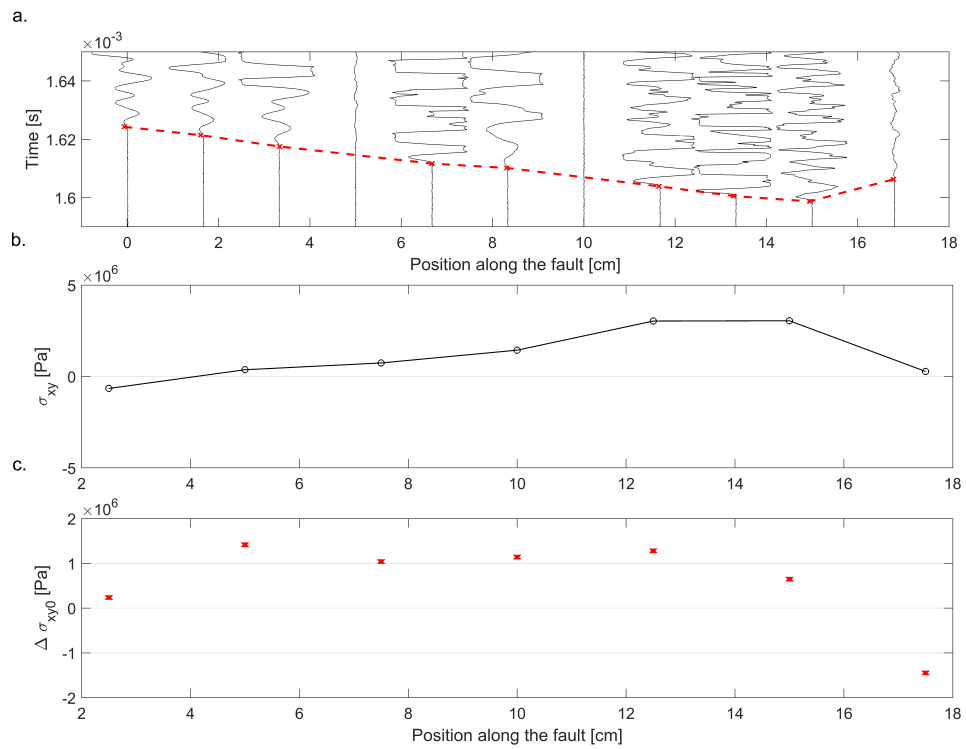


Figure 4.8: Test T10 (Gabro-Gabbro). (a) Rupture propagation front from acoustic data. (b) Stress distribution along the fault, prior the event. (c) Stress drops distribution recorded for each location along the fault.

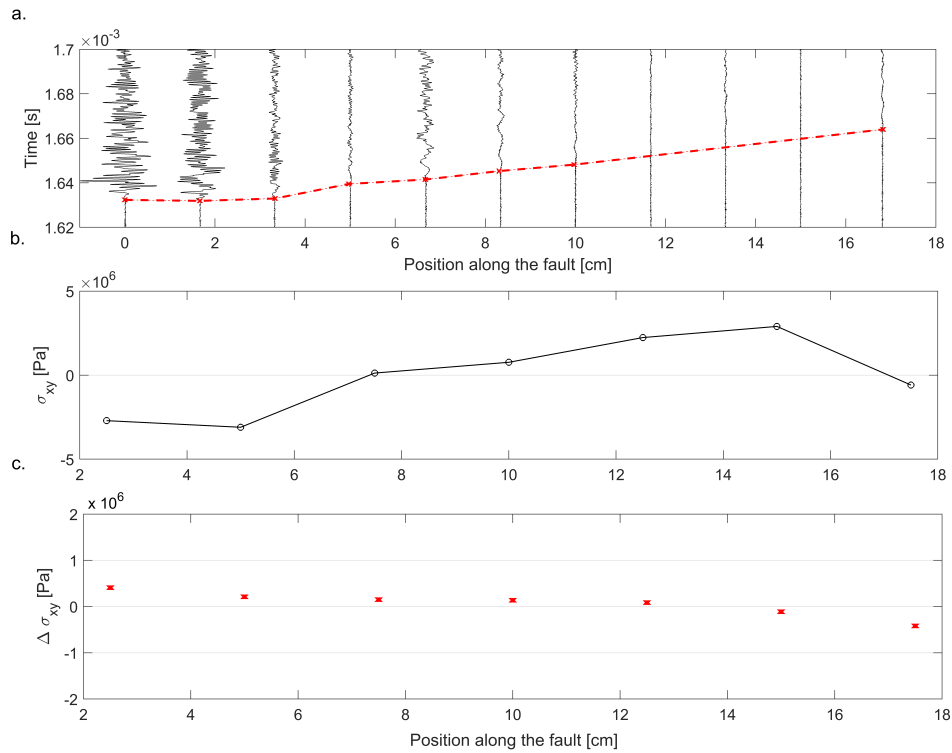


Figure 4.9: Test T13 (Granite-Granite). (a) Rupture propagation front from acoustic data. (b) Stress distribution along the fault, prior the event. (c) Stress drops distribution recorded for each location along the fault.

the end of the interface, which corresponds to a zone with higher shear stress than the rest of the fault. The rupture starts propagating at rupture speed towards the origin of the interface, while it seems to slow down, as soon as it starts on the right side. In fact looking at Fig.4.8 (b) on the right of the nucleation of the rupture the shear stress drops to zero. We can make the same observation for what concerns the stress drops. In Fig.4.8 (c) in fact, the corresponding stress drop is negative, which means that elastic energy is accumulated, therefore rupture is arresting.

The same observations can be done for experiment T13 whose rupture nucleates at a location  $x=2$  cm (4.5) .

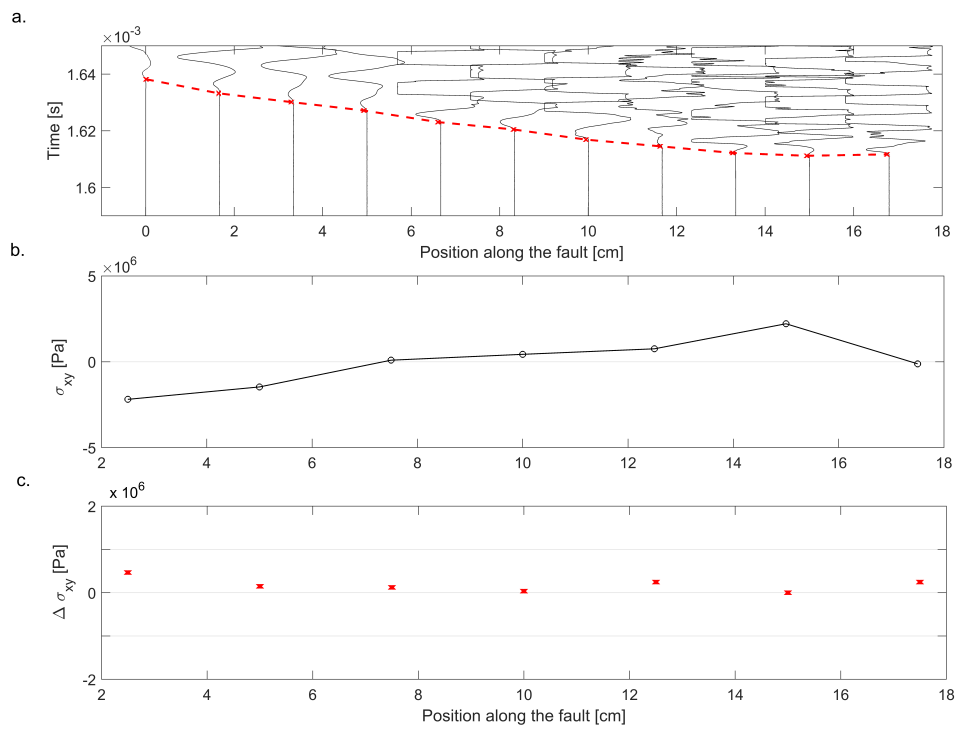


Figure 4.10: Test T12 (Gabro-Granite). (a) Rupture propagation front from acoustic data. (b) Stress distribution along the fault, prior the event. (c) Stress drops distribution recorded for each location along the fault.

In experiment T12 (the bi-material test) rupture nucleates at the edge of the interface. The stress drops are all positive, corresponding to a release of stress. In fact as can be seen in the acoustic data, the rupture wave front does not seem to arrest, propagating at the same velocity through the whole length of the interface with no attenuation or arrest of the rupture.

#### 4.4.2 Interpretation of stress heterogeneity

It can be noticed clearly from Fig. 4.8, 4.9, 4.10 that during the experiments there is a very strong heterogeneity of stress along the fault. This can be given by many factors, such as :

- Contact Area.
- Precursor events.
- Edge effect.

**Contact area.** The area we should account for (the real contact area) differs in a large amount from the nominal contact area. For this reason it would be important and interesting to be able to check for the real contact area through the whole motion in order to see how it affects the resulting slip. In this study it was not possible to measure the change of contact area between the two blocks.

**Relation between state of stress and foreshocks activity** It is known that the real contact area will change during slip, as studied in [33] and [32], depending on many factors. One of them; the precursory events. The occurring of these kind of events changes the stress distribution along the fault and the contact distribution as well [30]. Precursors happen to occur at values of friction way lower than the static one. They propagate through the fault arresting before reaching the end of it. For this reason there is no macroscopic sliding coupled with precursory events. In fact this is the main difference between precursor events and main events; the rupture tip arrests before passing through the entire fault in the first case, while the rupture tip makes it to the end of the fault producing slip, in the second case. These will make changes on the surfaces of the interface, causing a non uniform stress distribution.

A numerical study [30] showed how precursor events are related one to the other. In fact, given the first precursor event, the following one will be affected by the stress distribution left from the previous one and so for the following events. It has been shown how the peak stress from a stress distribution of a precursor is placed at the same length where the previous one had stopped. Moreover this stress singularity left from the previous event will affect the propagation velocity of the following one (most of the

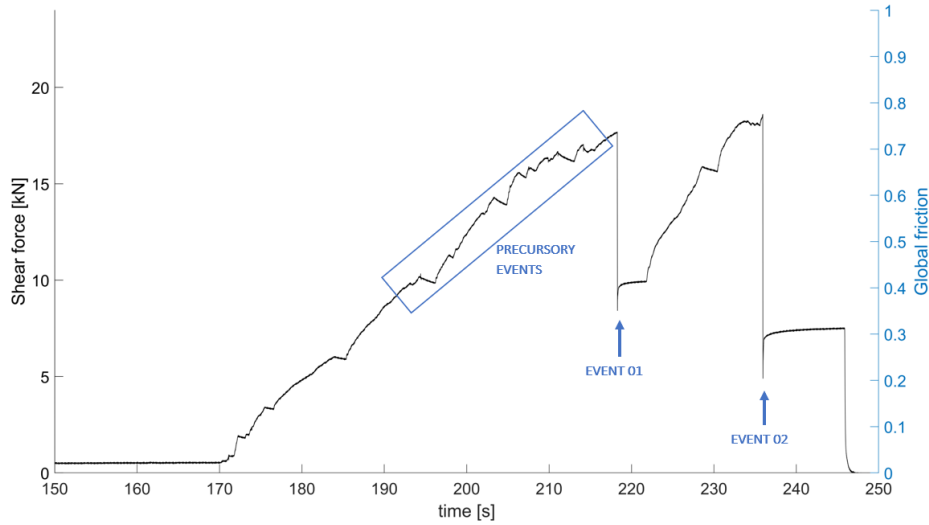


Figure 4.11: Evolution of shear stress and global friction with time. On the plot the precursory events and the main events are pointed out in blu.

times it will increase it). The propagation length will then increase with the number of precursors and with the increasing of shear load [27]. Only once this propagation length will equal the interface's length, then there will be macroscopic sliding or what is also called in [27] *bulk sliding*.

In Figure 4.11 it can be observed the shear stress evolution with time. In particular the shear stress is visible on the  $y_{left}$ -axis while the global friction is visible on the  $y_{right}$ -axis. As stated before, at global friction values lower than the static one, the first precursory events start occurring. For a friction value of about 0.4 the first precursor appears, followed by a series of small events occurring at higher global friction values. As soon as the global friction reaches its static value of about 0.77, the main event occurs (EVENT 01). As the shear stress keeps increasing there are no longer precursory events but only main events (EVENT 02). It is worth to notice that both main events occurs for the same global friction value, which correspond to the static value.

**Edge effect.** Between the various considered variables in addition to the occurrence of precursors (as already seen) a very important factor is the edge effect.

To this regard in our experiments, an important role was played by the constraint put on the left of the upper block (Fig A.3a). Apart from its essential role to prevent the upper block from rotating, it also brings not negligible stresses at the edge of the block. The stress distribution is in fact heterogeneous and heavily affected by this effect.

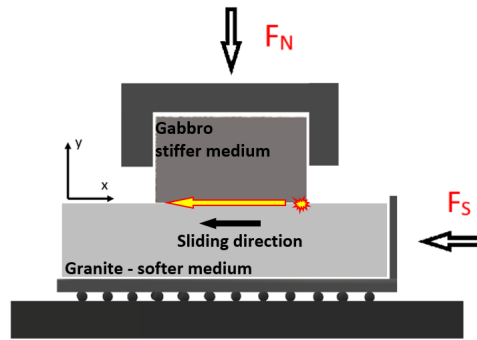


Figure 4.12: Scheme of rupture propagation in a bimaterial interface with softer medium put at the bottom.

#### 4.4.3 Effect of directivity.

We have seen (Fig. 4.7) how in bi-material interface the velocity of rupture is totally controlled by Granite. The rupture nucleating on the right of the fault, propagates in the sliding direction of the lower sample (Fig. 4.12).

This is in agreement with what numerically modelled in [3]. It is showed by numerical simulations that in faults with a material contrast (between the two sides of the interface) rupture will propagate in the slip direction of the more compliant material, with a rupture velocity closer to S wave velocity of the softer medium.

In this specific case the material contrast is about 10% and the softer medium is Granite with a deformation modulus of 66 GPa against Gabbro with a shear modulus of 88GPa. Even if in this case rupture velocity is higher than  $V_S$ , it still is controlled by the thresholds imposed by the softer medium. This could be an experimental evidence of what proposed and numerically investigated in [40, 3].

#### 4.4.4 Future prospects

**Apparatus set-up.** Despite my master project was mostly dedicated to obtaining the best configuration possible for Hopkinson 2D apparatus, still some work can be done in order for it to become a better machine.

In this paragraph I will list some adjustments that in my opinion are worthy.

- The machine should be made stiffer. By changing or adding some steel pieces in the configuration of the apparatus, it would become stiffer and would not deform under the solicitation of imposed loads.
- The mechanical recording system works at a recording frequency of 50 KHz. By improving this aspect and so making the frequency higher, it

could be possible to have a more detailed output of the strain distribution. It could then be possible to better study the rupture front and to compute the rupture velocity (which was possible so far through the acoustic recording system).

- In Figure A.3a it can be notice the presence of a stopper placed to the left of the upper sample. This was necessary during the experiments since it made the upper sample remain still during the sliding. Although this, as already explained, it generates some influencing effects on the stress distribution along the fault. It would be convenient to find out another way to secure the upper sample without the need to use a punctual tool.

**Experimental data.** For what concerns the next experiments to do it is necessary to be checked:

- The reproducibility of the actual data and results. To repeat most of the experiments again, to check for reproducibility and to give consistency to the first results.
- To keep testing different samples, of the same two materials, in order to make sure that the results are not given by a specific situation and condition but can be attributed to the elastic properties of the two chosen materials.

Of course these precautions were taken during this work, but the first experiments were all oriented to configure the machine set-up and so are not useful today in this direction.



## Chapter 5

# Conclusions

The overall results which emerge from this work are related to the influence of bi-material interface in the frictional behaviour of the interface itself and its dynamic response to solicitation. It came to light that the bi-material interface behaviour seems to respond to the already explained theories about directivity [40, 3].

The showed results demonstrate that while both materials exhibit velocity weakening behaviour, the frictional behaviour depends on the material contrast as well as of the roughness of the interface. If only one of the interface (with the same roughness on both sides) promote stable slip, the bi-material interface behaves stably. During dynamic rupture, the dynamic stress drops result in an average of both materials, which is a function of the elastic properties of both materials. During loading, the softer material is expected to accumulate larger strain than the harder material. Because of that, the release of strain will be larger in the slip direction on the side composed by the softer material. This larger release of strain explains at the first order the directivity effect of bi-material interface observed in nature. This result is in agreement with the preferential propagation of the rupture front observed during dynamic rupture experiments along bi-material interface.

The obtained results about the propagation of rupture at the onset of slip seem to confirm numerical results obtained by [3, 40]. The rupture nucleates at the edge of the fault and propagates preferentially in the slip direction of the softer medium, in this case represented by Granite.

To conclude, the experimental results highlighted that both asymmetry in roughness and lithology induce complexity in the rupture nucleation and propagation along fault interface. While an asymmetry in the roughness is the dominant parameter controlling the frictional behaviour of the interface, the asymmetry in lithology seems to control the propagation of the rupture front, as well as the associated wave radiation. These new results add further uncertainty to the formulation of physically based models of earthquake forecasting.



## Appendix A

# Hopkinson 2D configuration

In this appendix the configuration of Hopkinson 2D apparatus are shown.

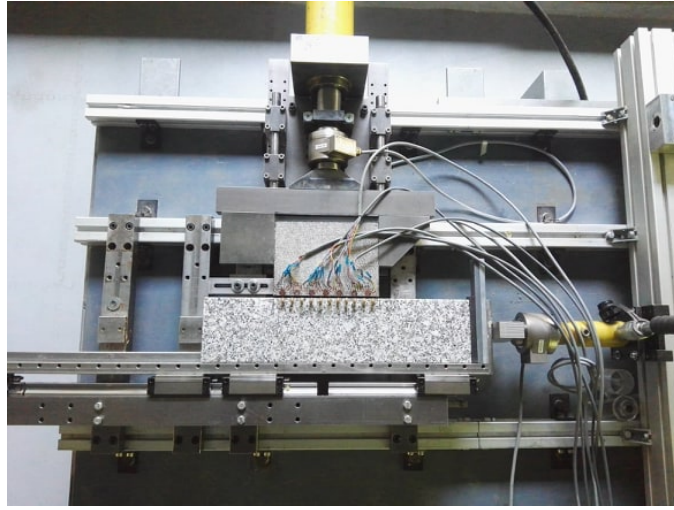


Figure A.1: Picture of the Hopkinson 2D apparatus, LEMR-EPFL.

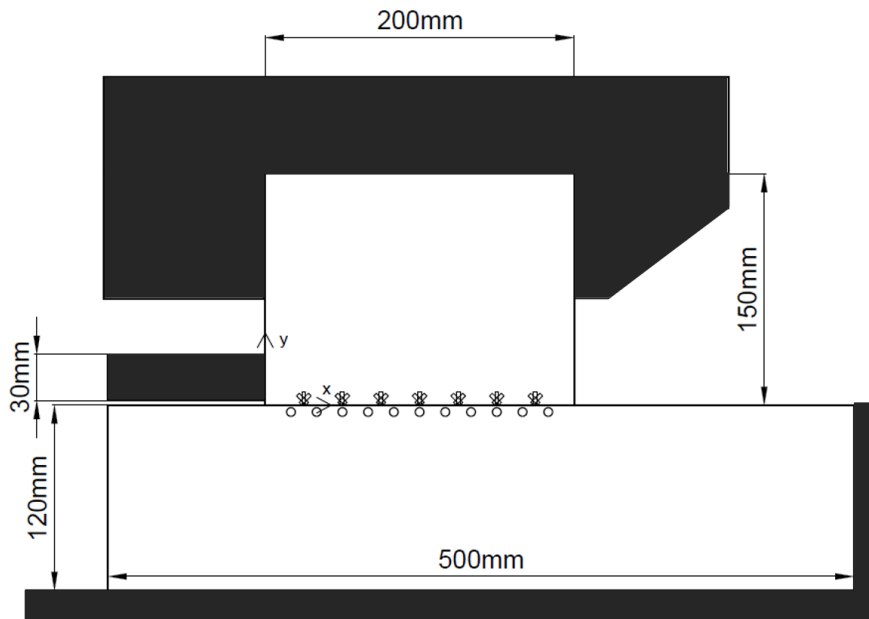


Figure A.2: Configuration of the Hopkinson 2D machine

(a) The upper block is kept still and is locked to the upper frame. The bottom block slides moved by a pump. A constrain is placed on the left of the upper block to prevent it from rotating during the experiment.

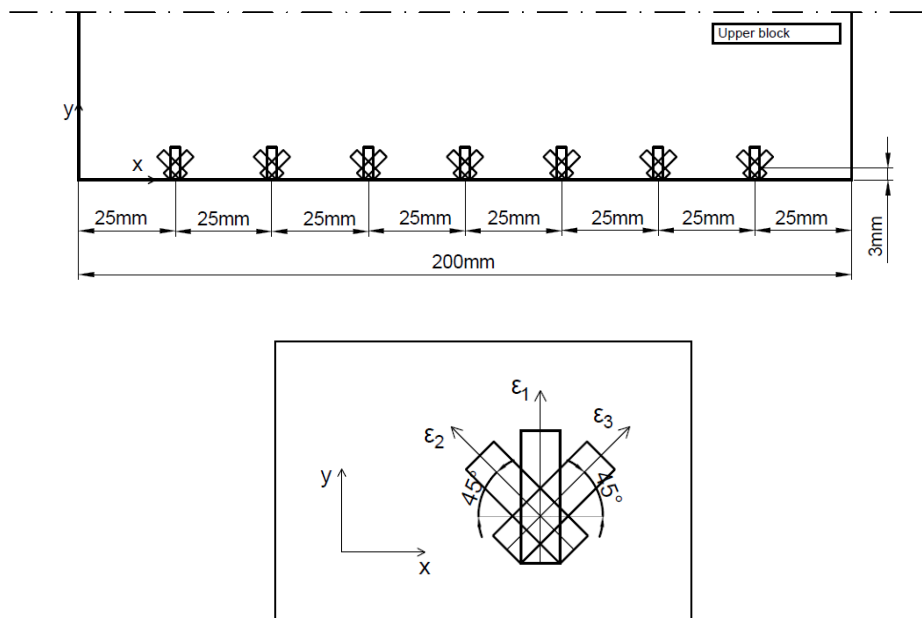


Figure A.4: (Top figure) Configuration of the mechanical sensors placed along the fault. Strain gages are glued on the upper block. (Bottom figure) Strain rosette used as mechanical sensor, which records strain in three directions;  $n_1$  which is parallel to  $y$ ,  $n_3$  which is inclined by 45 degrees and  $n_2$  which is inclined by 135 degrees.

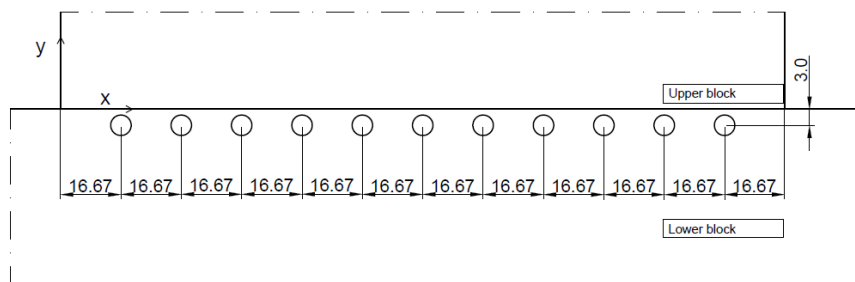


Figure A.5: Configuration of the acoustic sensors placed along the fault. Acoustic sensors are glued on the lower block. Unite measure: mm.

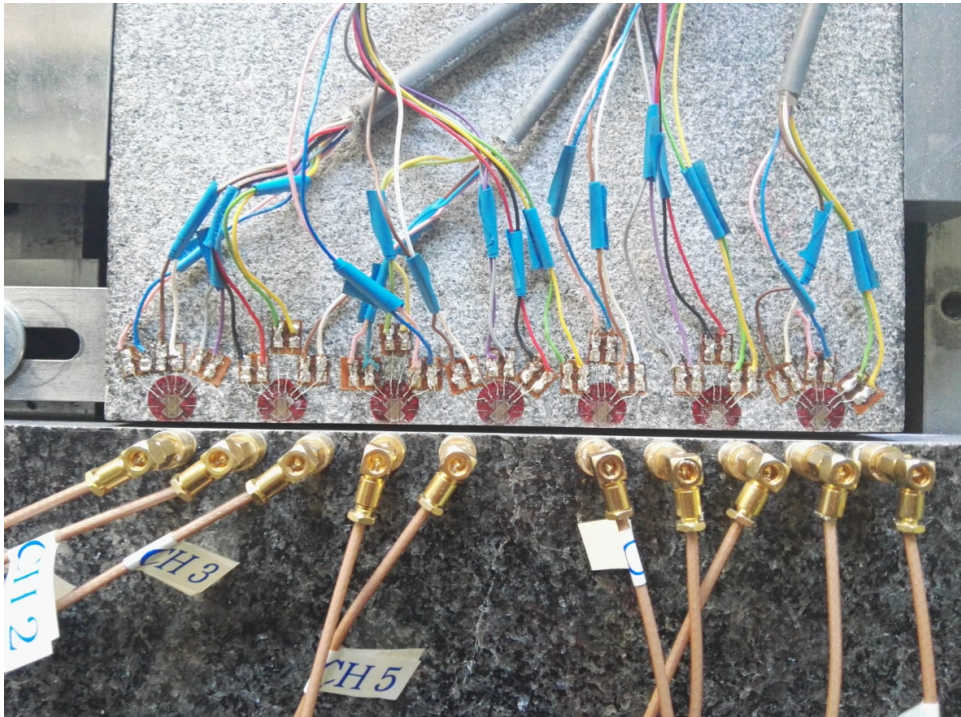


Figure A.6: Configuration of the mechanical and acoustic sensors. In this specific case the lower sample broke during the testing because of an alignment issue.

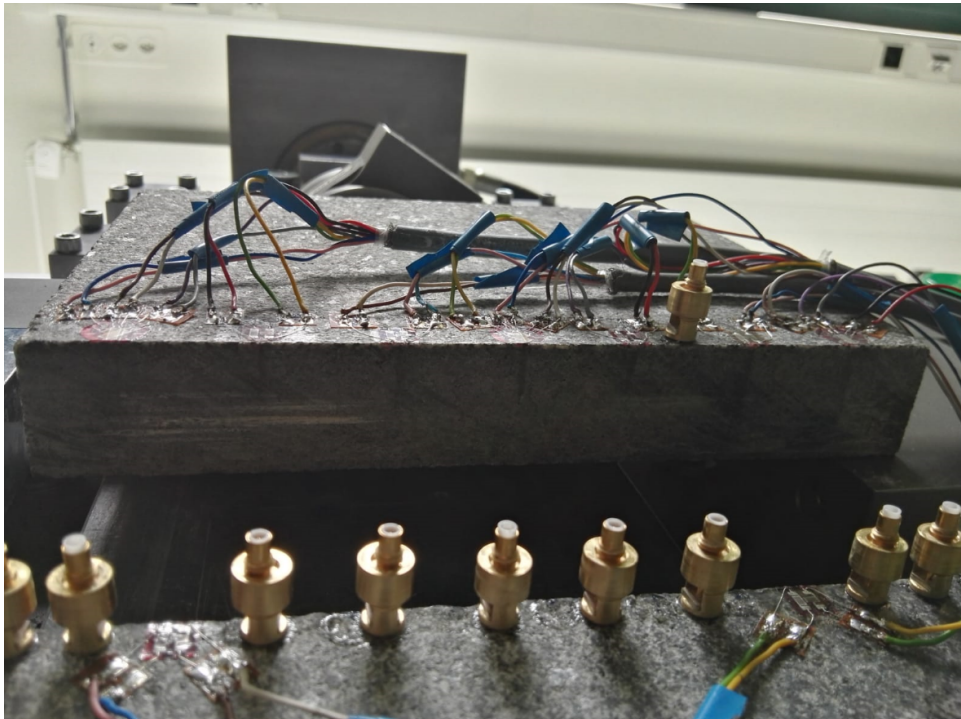


Figure A.7: Different configuration of the mechanical and acoustic sensors in order to choose the best one for our needs. On the thickness of the sample some stripes can be observed.

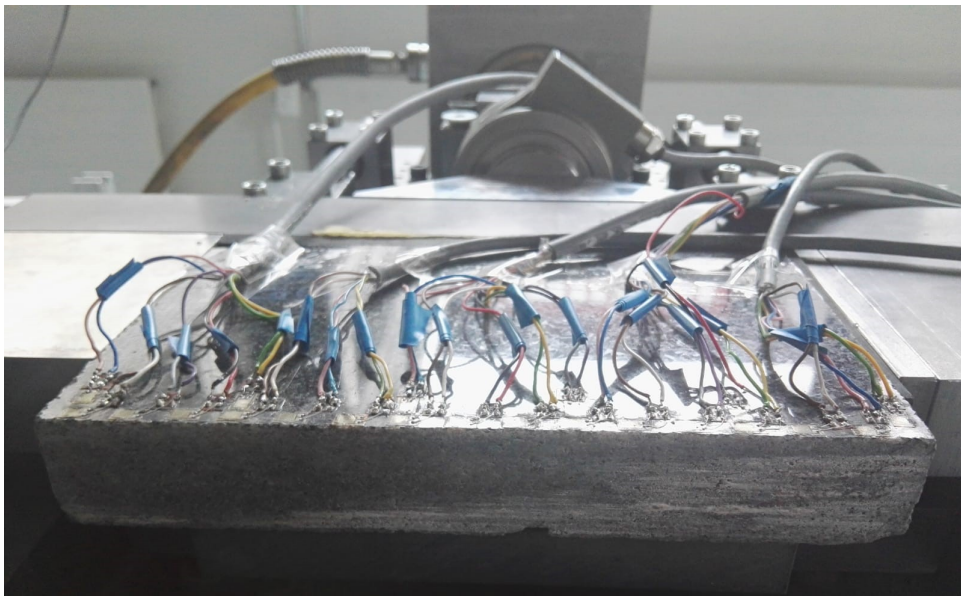


Figure A.8: Sample from one of the last experiments with the machine in its upgraded configuration. On the thickness of the sample some stripes can be observed. They are not distributed uniformly along the interface. This is sign of the influence of edge effect.

## Appendix B

# Hopkinson 2D - Defining strain and stress tensor.

### B.1 Strain tensor

It is known that a rotated system of strain can be related to the strain tensor that we are looking for  $(\varepsilon_{xx}, \varepsilon_{yy}, \varepsilon_{xy})$ . Since the orientation of the three gages is the one reported in Fig. B.1, the three angles to which we refer are:

$$\theta_1 = 90\text{degrees}$$

$$\theta_2 = 135\text{ degrees}$$

$$\theta_3 = 45\text{degrees}$$

$$\varepsilon_3 = \frac{\varepsilon_{xx} + \varepsilon_{yy}}{2} + \frac{\varepsilon_{xx} - \varepsilon_{yy}}{2} \cos(2 \cdot 45) + \frac{\varepsilon_{xy}}{2} \text{sen}(2 \cdot 45) \quad (\text{B.1})$$

$$\varepsilon_1 = \frac{\varepsilon_{xx} + \varepsilon_{yy}}{2} + \frac{\varepsilon_{xx} - \varepsilon_{yy}}{2} \cos(2 \cdot 90) + \frac{\varepsilon_{xy}}{2} \text{sen}(2 \cdot 90) \quad (\text{B.2})$$

$$\varepsilon_2 = \frac{\varepsilon_{xx} + \varepsilon_{yy}}{2} + \frac{\varepsilon_{xx} - \varepsilon_{yy}}{2} \cos(2 \cdot 135) + \frac{\varepsilon_{xy}}{2} \text{sen}(2 \cdot 135) \quad (\text{B.3})$$

By replacing all the angles we will have:

$$\begin{aligned} \varepsilon_3 &= \frac{\varepsilon_{xx} + \varepsilon_{yy}}{2} + \frac{\varepsilon_{xy}}{2} \\ \varepsilon_1 &= \frac{\varepsilon_{xx} + \varepsilon_{yy}}{2} - \frac{\varepsilon_{xx} - \varepsilon_{yy}}{2} \\ \varepsilon_2 &= \frac{\varepsilon_{xx} + \varepsilon_{yy}}{2} - \frac{\varepsilon_{xy}}{2} \end{aligned}$$

From the last equations the final strain equations can be defined as:

$$\varepsilon_{yy} = \varepsilon_1 \quad (\text{B.4})$$

$$\varepsilon_{xx} = \varepsilon_3 + \varepsilon_2 - \varepsilon_1 \quad (\text{B.5})$$

$$\varepsilon_{xy} = \varepsilon_3 - \varepsilon_2 \quad (\text{B.6})$$

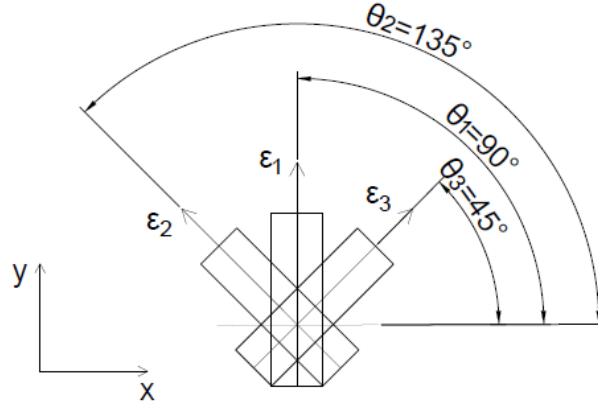


Figure B.1: Strain rosette in three directions;  $n_1$  which is parallel to  $y$ ,  $n_3$  which is inclined by 45 degrees and  $n_2$  which is inclined by 135 degrees.

## B.2 Stress tensor correction

The stress correction relies on a consideration regarding the stress equilibrium equations. In Figure B.2 it can be seen the stress distribution acting on a squared sample.

By writing the equilibrium in the  $x$  direction we get:

$$\sigma_{yx} + \frac{\partial \sigma_{yx}}{\partial y} dy + \sigma_{xx} + \frac{\partial \sigma_{xx}}{\partial x} dx - \sigma_{xx} - \sigma_{yx} = 0 \quad (\text{B.7})$$

$$\frac{\partial \sigma_{yx}}{\partial y} dy + \frac{\partial \sigma_{xx}}{\partial x} dx = 0$$

$$\frac{\partial \sigma_{yx}}{\partial y} dy = -\frac{\partial \sigma_{xx}}{\partial x} dx$$

Thanks to this observation the correction of the stress in the  $y$  direction changes from its initial formulation:

$$\sigma_{xy\text{corrected}} = \sigma_{xy} - \Delta y \frac{\partial \sigma_{xy}}{\partial y}$$

to the used one:

$$\sigma_{xy}^{y=0} = \sigma_{xy} + \Delta y \frac{\partial \sigma_{xx}}{\partial x}$$

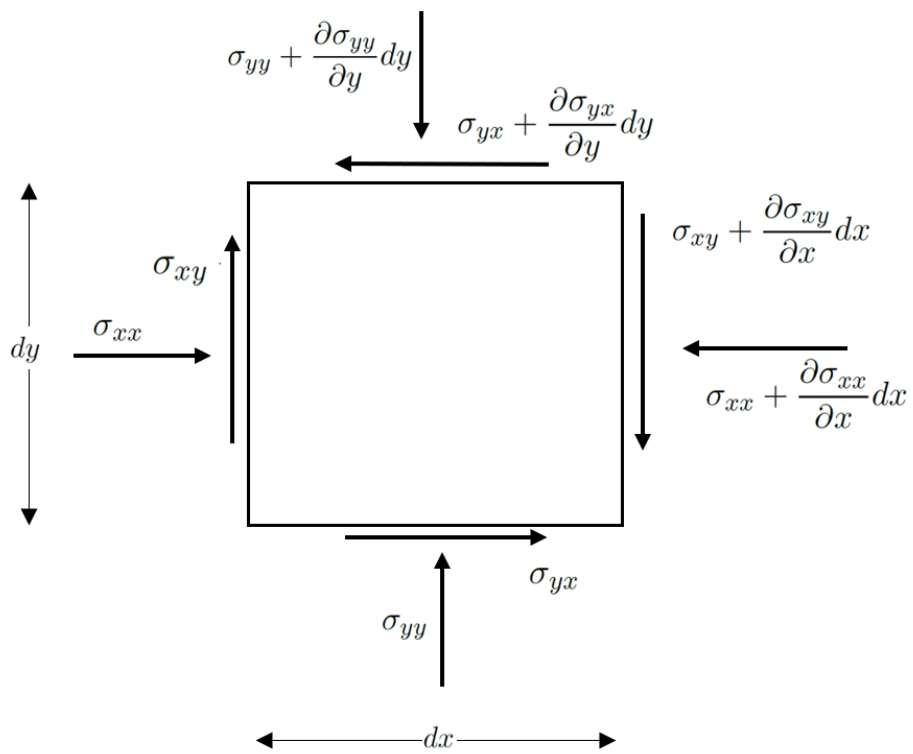


Figure B.2: Stress equilibrium.

62 APPENDIX B. HOPKINSON 2D - DEFINING STRAIN AND STRESS TENSOR.

# Bibliography

- [1] Hamid N Alsadi. *Seismic Hydrocarbon Exploration: 2D and 3D Techniques*. Springer, 2016.
- [2] Jean-Paul Ampuero and Allan M Rubin. “Earthquake nucleation on rate and state faults—Aging and slip laws”. In: *Journal of Geophysical Research: Solid Earth* 113.B1 (2008).
- [3] David J Andrews and Yehuda Ben-Zion. “Wrinkle-like slip pulse on a fault between different materials”. In: *Journal of Geophysical Research: Solid Earth* 102.B1 (1997), pp. 553–571.
- [4] E Bayart, I Svetlizky, and J Fineberg. “Rupture dynamics of heterogeneous frictional interfaces”. In: *Journal of Geophysical Research: Solid Earth* ().
- [5] Oded Ben-David, Gil Cohen, and Jay Fineberg. “The dynamics of the onset of frictional slip”. In: *Science* 330.6001 (2010), pp. 211–214.
- [6] RL Biegel et al. “Micromechanics of rock friction 1. Effects of surface roughness on initial friction and slip hardening in westerly granite”. In: *Journal of Geophysical Research: Solid Earth* 97.B6 (1992), pp. 8951–8964.
- [7] GN Boitnott et al. “Micromechanics of rock friction 2: Quantitative modeling of initial friction with contact theory”. In: *Journal of Geophysical Research: Solid Earth* 97.B6 (1992), pp. 8965–8978.
- [8] Michel Bouchon and Martin Vallée. “Observation of long supershear rupture during the magnitude 8.1 Kunlunshan earthquake”. In: *Science* 301.5634 (2003), pp. 824–826.
- [9] WF Brace and JD Byerlee. “Stick-slip as a mechanism for earthquakes”. In: *Science* 153.3739 (1966), pp. 990–992.
- [10] WF Brace and DL Kohlstedt. “Limits on lithospheric stress imposed by laboratory experiments”. In: *Journal of Geophysical Research: Solid Earth* 85.B11 (1980), pp. 6248–6252.
- [11] James D Byerlee and WF Brace. “Stick slip, stable sliding, and earthquakes—effect of rock type, pressure, strain rate, and stiffness”. In: *Journal of Geophysical Research* 73.18 (1968), pp. 6031–6037.

- [12] JD Das, AK Saraf, and S Panda. “Satellite data in a rapid analysis of Kashmir earthquake (October 2005) triggered landslide pattern and river water turbidity in and around the epicentral region”. In: *International Journal of Remote Sensing* 28.8 (2007), pp. 1835–1842.
- [13] James H Dieterich. “Constitutive properties of faults with simulated gouge”. In: *Mechanical behavior of crustal rocks: the Handin volume* (1981), pp. 103–120.
- [14] James H Dieterich. “Time-dependent friction and the mechanics of stick-slip”. In: *Rock Friction and Earthquake Prediction*. Springer, 1978, pp. 790–806.
- [15] Greg Hirth and Jan Tullis. “The brittle-plastic transition in experimentally deformed quartz aggregates”. In: *Journal of Geophysical Research: Solid Earth* 99.B6 (1994), pp. 11731–11747.
- [16] Satoshi Ide et al. “A scaling law for slow earthquakes”. In: *Nature* 447.7140 (2007), p. 76.
- [17] John Conrad Jaeger, Neville GW Cook, and Robert Zimmerman. *Fundamentals of rock mechanics*. John Wiley & Sons, 2009.
- [18] Carl E Johnson and David M Hadley. “Tectonic implications of the Brawley earthquake swarm, Imperial Valley, California, January 1975”. In: *Bulletin of the Seismological Society of America* 66.4 (1976), pp. 1133–1144.
- [19] Tracy Johnson, Francis T Wu, and Christopher H Scholz. “Source parameters for stick-slip and for earthquakes”. In: *Science* 179.4070 (1973), pp. 278–280.
- [20] D Kammer. “Slip fronts at frictional interfaces: A Numerical and Theoretical Study”. PhD thesis. PhD Thesis (EPFL Lausanne, 2014).
- [21] Hiroo Kanamori and Emily E Brodsky. “The physics of earthquakes”. In: *Reports on Progress in Physics* 67.8 (2004), p. 1429.
- [22] Raul Madariaga. “High frequency radiation from dynamic earthquake”. In: *Ann. Geophys.* 1 (1983), p. 17.
- [23] Chris Marone. “Laboratory-derived friction laws and their application to seismic faulting”. In: *Annual Review of Earth and Planetary Sciences* 26.1 (1998), pp. 643–696.
- [24] Chris Marone and SJD Cox. “Scaling of rock friction constitutive parameters: The effects of surface roughness and cumulative offset on friction of gabbro”. In: *pure and applied geophysics* 143.1-3 (1994), pp. 359–385.
- [25] Hiroyuki Noda and Toshihiko Shimamoto. “Constitutive properties of clayey fault gouge from the Hanaore fault zone, southwest Japan”. In: *Journal of Geophysical Research: Solid Earth* 114.B4 (2009).

- [26] Mitiyasu Ohnaka. “A constitutive scaling law and a unified comprehension for frictional slip failure, shear fracture of intact rock, and earthquake rupture”. In: *Journal of Geophysical Research: Solid Earth* 108.B2 (2003).
- [27] Michio Otsuki and Hiroshi Matsukawa. “Systematic breakdown of Amontons’ law of friction for an elastic object locally obeying Amontons’ law”. In: *Scientific reports* 3 (2013), p. 1586.
- [28] François X Passelègue et al. “From sub-Rayleigh to supershear ruptures during stick-slip experiments on crustal rocks”. In: *Science* 340.6137 (2013), pp. 1208–1211.
- [29] Ernest Rabinowicz. “The nature of the static and kinetic coefficients of friction”. In: *Journal of applied physics* 22.11 (1951), pp. 1373–1379.
- [30] Mathilde Radiguet et al. “Survival of heterogeneous stress distributions created by precursory slip at frictional interfaces”. In: *Physical review letters* 111.16 (2013), p. 164302.
- [31] James R Rice, Nadia Lapusta, and K Ranjith. “Rate and state dependent friction and the stability of sliding between elastically deformable solids”. In: *Journal of the Mechanics and Physics of Solids* 49.9 (2001), pp. 1865–1898.
- [32] Shmuel M Rubinstein, Gil Cohen, and Jay Fineberg. “Detachment fronts and the onset of dynamic friction”. In: *Nature* 430.7003 (2004), p. 1005.
- [33] SM Rubinstein, G Cohen, and J Fineberg. “Dynamics of precursors to frictional sliding”. In: *Physical review letters* 98.22 (2007), p. 226103.
- [34] Andy Ruina. “Slip instability and state variable friction laws”. In: *Journal of Geophysical Research: Solid Earth* 88.B12 (1983), pp. 10359–10370.
- [35] Christopher H Scholz. “Earthquakes and friction laws”. In: *Nature* 391.6662 (1998), p. 37.
- [36] Christopher H Scholz. *The mechanics of earthquakes and faulting*. Cambridge university press, 2002.
- [37] Alexandre Schubnel et al. “Photo-acoustic study of subshear and supershear ruptures in the laboratory”. In: *Earth and Planetary Science Letters* 308.3-4 (2011), pp. 424–432.
- [38] Zheqiang Shi and Yehuda Ben-Zion. “Dynamic rupture on a bimaterial interface governed by slip-weakening friction”. In: *Geophysical Journal International* 165.2 (2006), pp. 469–484.
- [39] Ilya Svetlizky and Jay Fineberg. “Classical shear cracks drive the onset of dry frictional motion”. In: *Nature* 509.7499 (2014), p. 205.

- [40] Johannes Weertman. “Unstable slippage across a fault that separates elastic media of different elastic constants”. In: *Journal of Geophysical Research: Solid Earth* 85.B3 (1980), pp. 1455–1461.
- [41] Shiqing Xu et al. “Strain rate effect on fault slip and rupture evolution: Insight from meter-scale rock friction experiments”. In: *Tectonophysics* (2017).